Nano Today 24 (2019) 120–140

Contents lists available at ScienceDirect

Nano Today

journal homepage: www.elsevier.com/locate/nanotoday

Gold nanoparticles in biological optical imaging

Yue Wu [a], Moustafa R.K. Ali [a,*], Kuangcai Chen [b], Ning Fang [b,*], Mostafa A. El-Sayed [a,*]

[a] School of Chemistry and Biochemistry, Georgia Institute of Technology, Atlanta, Georgia, 30332, USA
[b] Department of Chemistry, Georgia State University, P.O. Box 3965, Atlanta, Georgia, 30302, USA

ARTICLE INFO

Article history:
Received 16 October 2018
Received in revised form 1 December 2018
Accepted 24 December 2018
Available online 5 January 2019

Keywords:
Gold nanoparticles
Optical imaging
Bioimaging
Resolution
Penetration depth
Plasmonic effect
Microscopy
Diagnosis

ABSTRACT

Optical imaging represents one of the most essential tools in biological studies. Although with great advances, bio-optical imaging still suffers from problems such as resolution, sensitivity, speed, and penetration depth. Due to the unique optical properties of gold nanoparticles (AuNPs), *i.e.,* surface plasmon resonance, AuNPs can be readily used to enhance optical imaging based on their absorption, scattering, fluorescence, Raman scattering, *etc*. Here, we include the most recent achievements and challenges associated with using AuNPs to improve resolution and sensitivity in biological imaging *in vitro* and *in vivo*. The application of AuNPs in the following three aspects were discussed: **1)** Direct visualization of AuNPs inside the biosystems using i) dark field (DF) microscopy, ii) differential interference contrast (DIC) microscopy, and iii) other techniques, such as interferometric scattering (iSCAT) microscopy and photothermal imaging. Additionally, since orientation and rotational motions are closely related to various biological processes, we also summarized the recent advances of optical imaging methods in the rotational and orientation tracking of AuNPs. **2)** Monitoring of biomolecular events and physiological processes using i) surface-enhanced Raman spectroscopy (SERS) and ii) plasmon enhanced fluorescence (PEF) for ultra-sensitive detection of biomolecules, including proteins, metabolites, DNA, RNA, *etc.* **3**) *In vivo* deep tissue imaging using i) two-photon and/or multi-photon imaging, ii) optical coherence tomography (OCT), and iii) photoacoustic (PA) imaging for disease diagnoses, such as detecting tumors and other diseases in eye, brain, and bone. In conclusion, based on our literature study, AuNPs-assisted bioimaging acts as a promising tool in exploring fundamental biological questions and early diagnosis of diseases.

Contents

* Corresponding authors.
E-mail addresses: mali43@gatech.edu (M.R.K. Ali), nfang@gsu.edu (N. Fang), melsayed@gatech.edu (M.A. El-Sayed).

https://doi.org/10.1016/j.nantod.2018.12.006
1748-0132/

Introduction

Gold has been a mainstay of science and technology for thousands of years. Gold is a rather non-reactive metal, but when the size is reduced to the nanometer scale, its properties completely change due to the drastic changes in its electron behavior at this length scale [1]. Colloidal gold nanoparticles (AuNPs) are one of the most stable nanoparticles and present fascinating properties. The use of AuNPs possibly dates back to the 4^{th} or 5^{th} century B.C. in Egypt and China for decoration and medical treatment purposes [2]. One famous example in history is the Roman Lycurgus Cup, which appears green when exposed to reflected light and red to transmitted light due to the unique properties of AuNPs embedded within the glass. In a well-known lecture by Faraday in1857, a ruby solution of colloidal gold was prepared by reduction of ionic gold in an aqueous solution, and the interaction between AuNPs and light was explored [3]. In the last decade, various methods have been developed for synthesizing AuNPs with different shape and sizes and their optical properties have been extensively explored [4–9]. With the development of gold nanotechnology, AuNPs play important roles in a wide range of fields, from catalysis and energy to biology and medicine [6,10–14].

The unique properties of AuNPs originate from surface plasmon resonance (SPR). When light is applied to AuNPs at the specific wavelengths, electrons begin to oscillate in resonance with the frequency of light due to the interaction between the electromagnetic field of light and the conduction electrons of AuNPs [15]. The SPR gives AuNPs unique optical properties including their large absorption and scattering cross-sections. The SPR wavelengths of AuNPs are dependent on their size, shape, and local dielectric surroundings. In addition, AuNPs can be easily surface-modified with proteins, peptides, oligonucleotides, and many other compounds, while still maintaining their optical properties. The easy surface modification of AuNPs enables their targeting of specific subcellular locations and allows for the enhanced efficacy in imaging [16,17]. Furthermore, one of the greatest attributes of AuNPs that has set them above their metallic particle counterparts is their chemical inertness, and it is because of their low toxicity that AuNPs are often used in biological systems. The above properties, including plasmonic properties, targeting, and bio-compatibility have turned AuNPs into incredibly useful nanomaterials with a wide range of chemical and biological applications, specifically in bio-imaging [18–21].

Using a microscope, Robert Hooke (in 1665) and Anton van Leeuwenhoek (in 1674) observed the images of "cell", opening the door of cell biology. The development of optical microscopes during the last 350 years enables us to see more microscale details in the biological system. One recent noteworthy progression is the development of optical super-resolution microscopy, which allows the observation of macromolecules in live cells down to nanoscale level and was awarded the 2014 Nobel Prize in Chemistry. Although with great advances, bio-optical imaging always has coupled strengths and weaknesses regarding resolution, sensitivity, speed, and penetration depth.

Recently, there has been a great deal of research concerning the advancement of optical imaging using AuNPs due to their unique plasmonic properties [22]. The first question that arises is how to clearly "visualize" the AuNP probes inside cells [23,24]. The scattering signal from AuNPs is usually much stronger than the scattering background from cells and tissues, making dark field (DF) microscopy a viable choice for reporting the existence of AuNPs within biological systems. Differential interference contrast (DIC) microscopy uses two interference light beams to generate contrast for optical path differences, allowing for the simultaneous imaging of nanoparticles and cellular components, such as nuclei, vesicles, and microtubules. Interferometric scattering microscopy (iSCAT) relies on the interference between a reference light and light scattered by the specimen in the medium to produce a high interferometric contrast image that can be obtained after the removal of static imaging background, allows sensitive and precise imaging of AuNPs with improved spatiotemporal resolution. In addition, the light absorbance by AuNPs could be converted to heat, which can be used for photothermal imaging.

Molecular orientation and rotational motion are commonly involved in many important biological processes, such as the stepping motion of motor proteins, self-rotation of F_1-ATP synthase, Dynamin scission during clathrin-mediated endocytosis, and DNA twisting during polymerization and depolymerization. Optically anisotropic AuNRs became ideal orientation and rotational probes thanks to their geometrically confined SPR, which results in anisotropic absorption and scattering. With the recent development of advanced optical microscopic methods, AuNPs have been extensively used to investigate the rotational dynamics associated with essential biological events. In this review, several AuNP-assisted optical imaging methods in rotational tracking are discussed.

In addition to visualizing the AuNPs inside the cells, a second question that comes to mind is how AuNPs could improve the detection of biological events. A useful by-product of AuNP light scattering is the enhanced Raman signals for molecules [25]. Raman spectroscopy is a powerful tool for analyzing the species within a biosystem as it provides the chemical fingerprint of the molecule [26]. AuNPs can greatly enhance the Raman signal of a molecule. The surface-enhanced Raman scattering (SERS) obtains more than 10 orders of signal enhancement, allowing for ultra-sensitive single molecule level detection (down to 10^{-15} M). Additionally, compared to other imaging methods, SERS can provide more chemical bond/structure information. As the SERS peaks appear sharper compared to other detection methods such as fluorescence, higher accuracy in detection can be accomplished. *In vivo* SERS imaging for tumor diagnosis and therapy is a recent trendy development, which is bringing SERS into many clinical imaging applications. Besides SERS, plasmon-enhanced fluorescence (PEF) can also be acquired on the surface of AuNPs, as the strong coupling between the fluorophore and the SPR could dramatically change the fluorescence emission [27–29]. PEF greatly aids fluorescence imaging by achieving higher sensitivity and spatial resolution. Furthermore, the recently emerging field of fluorescence-emitting gold nanoclusters (AuNPs below 2–3 nm) enables the direct fluorescence imaging of nanoparticles without conjugation of fluorophores.

Finally, for most optical microscopic techniques, the imaging depth is limited to several 100 μm of tissue depth due to the strong scattering from the tissue. Acting as contrast-enhancing agents, AuNPs have been widely studied for assisting in *in vivo* optical imaging such as two-photon or multi-photon luminescence, optical coherence tomography (OCT), photoacoustic imaging, *etc*. The tissue penetration depths of these methods can reach mm to cm.

This review article serves to introduce the recent advancements of using AuNPs in bioimaging and sensing to discuss technique developments and to address fundamental questions regarding the enhancement of bioimaging with AuNPs.

Direct visualization of gold nanoparticles in biological systems

Recent innovations in optical imaging, including DF, bright field, DIC microscopies, photothermal and photoluminescence detection methods, *etc*., enable the visualization of single AuNPs interacting with the biological systems. The development of these methods has enhanced our ability to detect, localize, and track the dynamics of individual AuNPs and/or their aggregates and has broadened the understanding of bio-nano interactions in terms of the protein corona formation, membrane binding and diffusion, internalization, and trafficking of nanoparticles within cells [30–32]. Furthermore, AuNPs can be used as both diagnostic and therapeutic agents. In this section, we will mainly focus on the recent advances in DF, DIC, iSCAT, and photothermal microscopies as well as their applications in the study of bio-nano interactions.

Dark field (DF) microscopy

DF microscopy, a scattering-based technique, produces a bright image of the specimen on a dark background. The strong scattering signal of AuNPs is attributed to their high scattering coefficients (~5 orders of magnitude higher than conventional fluorescent dyes) [33].

Imaging gold nanoparticles inside cells

Extensive work has been conducted regarding the use of DF microscopy to track the intracellular locations and behavior of AuNPs inside cells, such as the examination of AuNP uptake [34], the evolution of AuNP clusters in live cells (based on their color change [35,36], corresponding to different cluster sizes and cellular locations, as shown in Fig. 1A), and the endocytosis and subsequent transport along the microtubules [36–38]. Rosman et al. reported a study regarding the intracellular behaviors of nanoparticles by quantifying the number of AuNPs within cells and the degree of aggregation using both optical DF microscopy and high-resolution TEM. They were able to employ the combined techniques to analyze the uptake of AuNPs with different shapes and surface coatings into epithelial cells [34].

AuNPs trafficking along microtubules. Nan et al. developed a novel strategy for the tracking of AuNPs in 2D with **~1.5 nm spatial precision and 25 μs time** resolution by utilizing a quadrant photodiode to record the positions of the AuNPs [37]. This technique is able to clearly resolve the 8 nm individual steps of cargoes that are carried by kinesin, as well as the 12, 16, and 20 nm steps by dynein with high localization precision and high time resolution (Fig. 1B) [37]. Schneider et al. visualized the AuNP-loaded motor proteins traveling along the microtubule using a parabolically-shaped quartz prism-based widefield total internal reflection (TIR) illumination design that allows the detection of single-molecule fluorescence and single-particle scattering with the same setup and high S/N ratios. Their results demonstrated sub-nanometer localization accuracy for the scattering of 40 nm AuNPs, and they imaged the characteristic 8-nm walking step distance of individual kinesin-1 motor proteins along the microtubules [38].

Imaging biological processes.. Additionally, DF microscopy incorporating AuNPs can be used for understanding biological processes. El-Sayed and co-workers have reported Au nanospheres functioning as DF probes for cell division [39]. AuNPs localized in the nuclear region were tracked in real time during the mitosis of a HSC-3 cancer cell (Fig. 1C). In addition, real-time tracking of virus-cell interactions was assisted by AuNPs in order to understand the respiratory syncytial virus infection of HEp-2 cells (Fig. 1D). Streptavidin (SA)-biotin binding chemistry, a study where AuNPs and virus particles are respectively modified with SA and biotin, allows for the stable binding of AuNPs to viruses without affecting their virulence [40]. A possible concern regarding this type of study is the endocytosis of free AuNPs (unbound to virus) that will complicate the detection.

Measuring biomolecular dynamics and mechanics

While the location of an individual, isolated nanoparticle can be determined by DF microscopy with nanometer spatial precision due to the strong scattering signal, the resolution for determining the distances between two identical particles is low (limited by the diffraction limit to ~250 nm). Thanks to the SPR shift with the change of inter-particle distances, the detection of close distances between AuNPs is possible. Using this method, the nanometer-level distance between two proteins inside cells was able to be measured, as reported by Rong et al. [41]. As shown in Fig. 2A, in the top case, AuNP-labeled fibronectin-integrin protein complexes are largely separated (separation distance Δ' is larger than AuNP diameter D), and the SPR of the AuNPs are same as individual particles (530 nm). However, in the bottom case, the proteins are close to each other (separation distance Δ" is smaller than AuNP diameter D), and the plasmon coupling between individual AuNPs causes a red shift of the SPR to 580 nm. This method can improve the resolution of optical imaging by more than one order of magnitude, where the detection threshold of 15 nm can be obtained with the chosen 530 nm/580 nm filter [41]. However, a possible concern regarding this type of study in general is the aggregation of AuNPs inside cells, which will cause a similar red-shift, and it is difficult to differentiate if this shift is from the small distance of the separated proteins or the AuNP aggregation. Aside from measuring protein distances inside the cells, Yeung and co-workers recently measured the cell

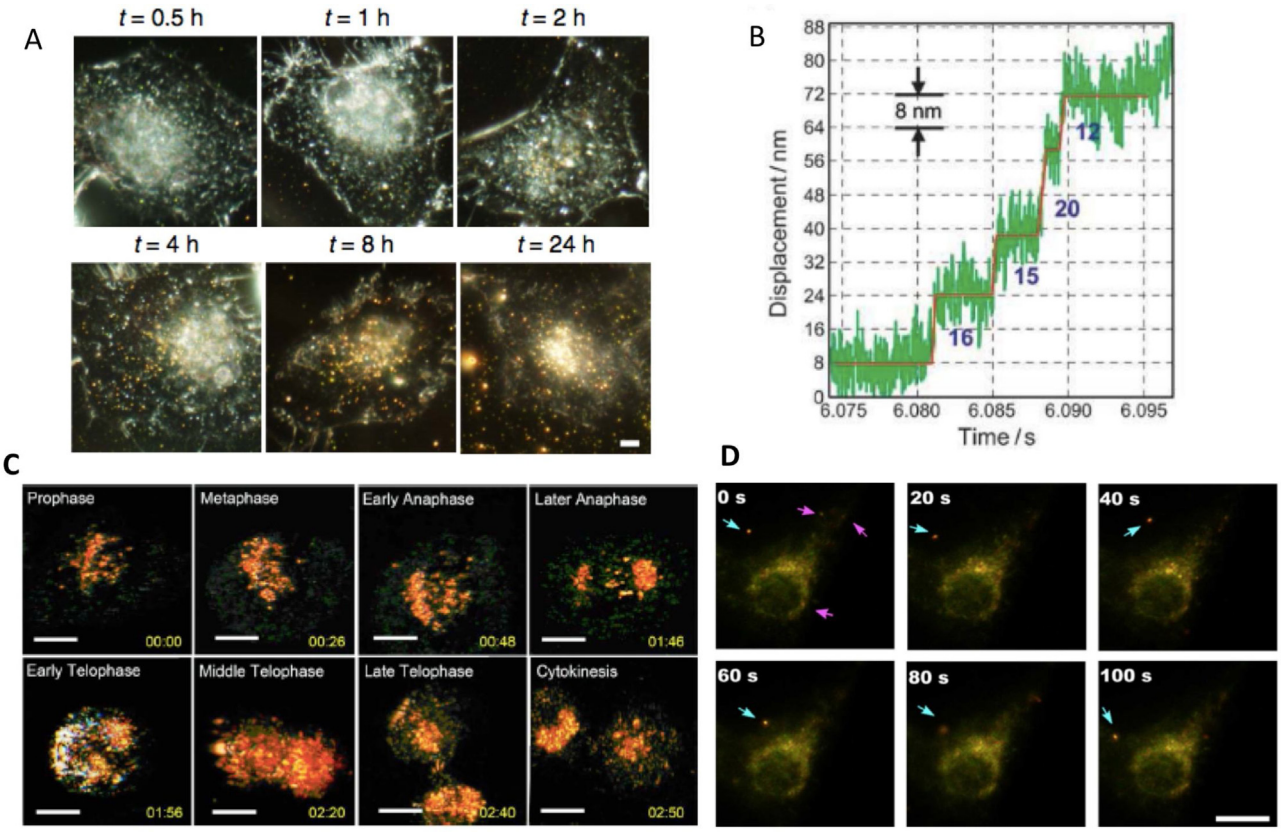

Fig. 1. (A) Dark field (DF) microscopy showing the evolution of AuNP color in HeLa cells at the different durations (0.5–24 h) of incubation. Printed with permission from Springer Nature [36]. (B) The walking steps of cargoes detected that are carried by dynein with ~1.5 nm spatial precision and 25 μs time resolution. Printed with permission from John Wiley and Sons [37]. (C) Human oral squamous cell carcinoma (HSC-3) cell division process (prophase to cytokinesis) visualized by the AuNPs. Printed with permission from SPIE [39]. (D) Real-time tracking (0–100 s) of AuNPs labeled respiratory syncytial virus (indicated by blue and red arrows) infecting HEp-2 cells. Printed with permission from Springer Nature [40].

mechanical force using AuNPs and DF microscopy according to the color change [42]. Mechanical force plays important roles in cell signaling for various physiological functions [43], and AuNP-based optical fluorescence imaging was previously developed to measure small forces in cells [44,45]. As shown in Fig. 2B, by using a single plasmonic nanospring that attaches to the cell surface integrins and DF microscopy, the force applied on the spring can result in an SPR alteration, which can be used for real-time measure of forces in live biological systems. In addition, based on the distance-related color change, AuNRs and DF microscopy also enables quantitative imaging of mRNA splice variants in live cells. The probes that Lee et al. developed consist of 40 nm AuNPs functionalized with two oligonucleotides that can match to specific mRNA sequences (BRCA1 mRNA). As shown in Fig. 2C, the formation of a dimer could cause the SPR color to be red-shifted and intensity to be greatly enhanced. The location and number of dimers can thus be determined and quantified using the signal intensity and spectral peak shift by DF microscopy [46].

AuNRs have also been used to detect the dynamic behavior of proteins. Lambertz et al. monitored the oscillations of the MinDE protein wave propagation on *Escherichia coli* (*E. coli*) membranes [47]. As shown in Fig. 2D, the attachment of proteins MinD and MinE to the membrane can be detected by the shifting of the AuNR SPR ($\Delta\lambda$), which exhibits four phases. Enzymatic reactions in live cells can also be indicated by the SPR shift. A single AuNP was used by Zhang et al. as a real-time probe for the detection of the NADH-dependent intracellular metabolic enzymatic pathways [48]. The NADH-mediated reduction of Cu^{2+} onto AuNPs that form Au@Cu core-shell nanoparticles causes a red-shift of the SPR spectra of AuNPs (Fig. 2E). The higher red-shift of the peak indicates the higher NADH concentration.

In vivo *dark field imaging*

Although widely used in single cell imaging, the DF technique has several obstacles that inhibit its application on animal imaging. Light scattering from surrounding tissue is a widely noted drawback of DF microscopy, and it limits the use of this imaging method within deep tissue. The current *in vivo* DF imaging still exclusively works on the tissue slides sections, such as for observing the AuNPs distribution in tumors, the tumor's vasculature and organs [49,50]. To characterize the biodistribution profiles of AuNPs, SoRelle et al. developed adaptive algorithms for the analysis of hyperspectral DF images that achieve improved sensitivity and specificity with the capability of identifying single nanoparticles in *ex vivo* mouse tissue sections [50]. The dependence on size for the optimal uptake of nanoparticles into brain tissue was highlighted by Betzel et al. who used DF images to display the enhanced internalization of glucose-coated 5 nm AuNPs into exosomes in comparison to 20 nm nanoparticles in brain slide sections. AuNPs were then used as tracking probes to map the movement of intranasally administered exosomes through mice focal brain ischemic-like damage, confirming their valuable use as contrast agents in DF microscopy applied to exosome labeling and exosome-based treatment [51].

Plasmon helps improve spatial resolution

DF imaging is yet another method that suffers from the optical diffraction limit, and as such, improving the resolution has been a huge subject of research in recent years [19,52,53]. Fig. 3A shows

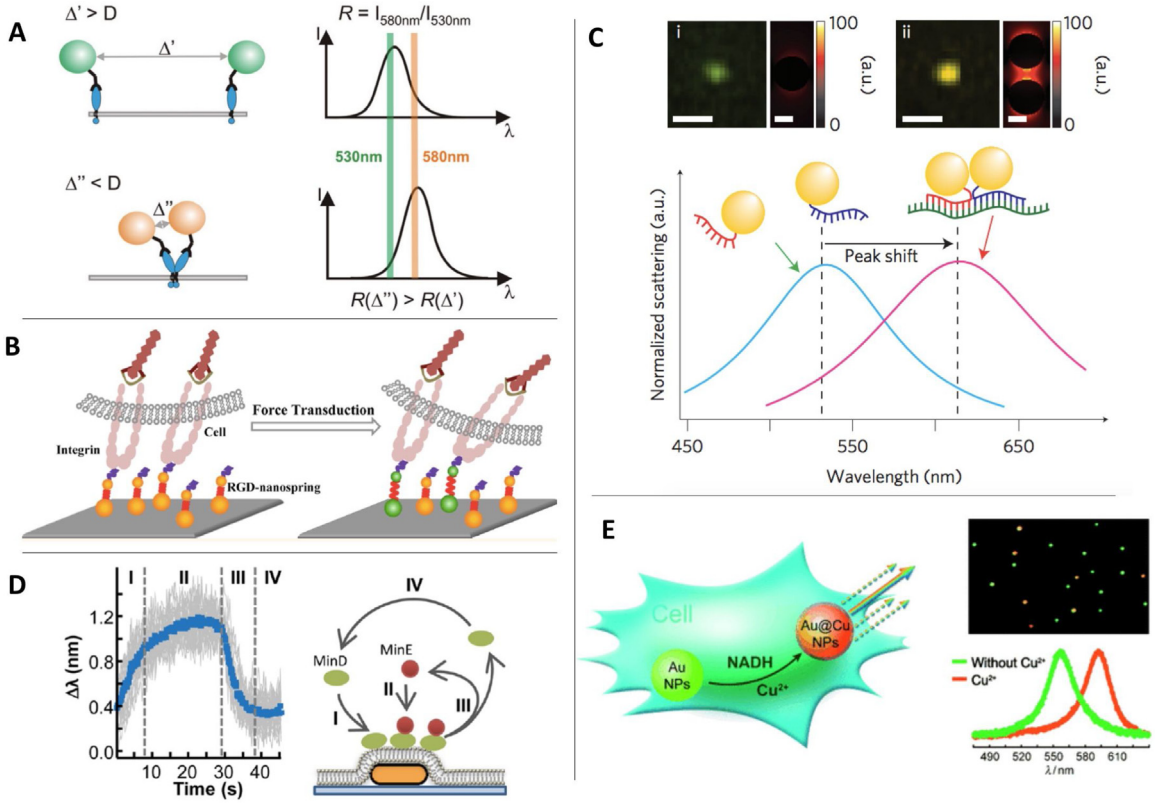

Fig. 2. (A) Schematic of using surface plasmon resonance (SPR) wavelength shift to determine the distance of proteins (labeled by AuNPs) in live cells. If the separation distance (Δ') is larger than AuNP diameter D, the SPR band is at about 530 nm. If separation distance (Δ") is smaller than D, the SPR band could ref-shift to 580 nm. Printed with permission from American Chemical Society [41]. (B) Schematic of using SPR shift to determine the cellular mechanical forces. Printed with permission from American Chemical Society [42]. (C) AuNRs enables quantitative imaging of mRNA splice variants in live cells. The real-color images (top) and spectra of monomer and dimer from mRNA splice variants (bottom). Printed with permission from Springer Nature [46]. (D) AuNR and dark field microscopy for monitoring protein dynamic behavior on membranes (reflected on the AuNR SPR shift, Δλ, in stage I, II, III and IV during a cycle). Printed with permission from American Chemical Society [47]. (E) AuNPs with Cu^{2+} detection of NADH-dependent intracellular metabolic enzymatic pathways. The deposition of Cu^{2+} on AuNPs causes red shift of SPR. Printed with permission from John Wiley and Sons [48].

a traditional working principle of DF microscopy. For selective illumination and decreasing background, Noji and his coworkers developed a simple DF microscope that employed perforated mirror and objective-based TIR. Due to the TIR illumination applied on a thin layer, a low background was achieved (Fig. 3B–D). The system was applied to visualize the rotation of F_1-ATPase attached to 40 nm AuNPs at 1–2 nm spatial resolution and 9.1 μs temporal resolution with 120° steps and short catalytic dwells on μs-to-ms timescales [54]. Another study established a super-resolution imaging of AuNPs with enhanced DF imaging based on wavelength modulation [55]. Individual bandpass filters were used to reduce the interference and to differentiate the adjacent AuNP, AuNR and silver nanoparticle at specific SPR wavelengths. The 2D Gaussian fitting algorithm was used to localize the nanoparticles with nanoscale precision.

While such techniques only reduced the interference of overlapping scattering in two dimensions, a very recent study has seen the development of DF imaging that accurately shows the 3D distribution of AuNPs within cells through the reduction of all background interference. This technology, known as orientation-dependent localization microscopy (ODLM), relies on the principle of cross-polarization microscopy to isolate the scattering of polarization-sensitive AuNRs, while intracellular structures incapable of depolarizing light are largely eliminated (Fig. 3E). Not only does this type of imaging allow for greater accuracy in pinpointing the localization of AuNPs within cells, but it also shows their specific orientation on an individual particle level without the interference of scattering from 3D subcellular structures [56].

Differential interference contrast (DIC) microscopy

DIC microscopy utilizes two-beam interferometry in which objects cause a phase shift of the light beams, producing a pseudo-3D, shadowcast image (Fig. 4A). DIC microscopy allow for the direct observation of many subcellular organelles, such as microtubules, in unstained living cells with sufficiently high contrast. DIC microscopy has been extensively used in cell biology to study microtubule assembly/disassembly dynamics, motor protein-microtubules binding, organelle trafficking in axon, cell division, and even intact organisms such as embryos [58–61]. AuNPs used as contrast agents in DIC microscopy allows for the imaging of nanoparticles and cellular features simultaneously [62]. Thanks to the high absorption and scattering cross-sections arising from the SPR as well as the excellent photostability of the AuNPs, relatively low illumination light intensity (standard halogen lamp is commonly used) is sufficient for DIC imaging of AuNPs in the cellular environment. This enables the continuous observation of dynamic bio-nano interactions for long periods of time with minimal disruption.

Three-dimensional selective imaging of gold nanoparticles

The challenge of differentiating AuNPs probes from small subcellular features, especially small intracellular spherical vesicles, in DIC images can be relatively easily circumvented by wavelength-dependent DIC microscopy to selectively image AuNP probes in live cells [63]. This method can turn "on/off" the AuNP signals by simply applying two bandpass filters in the light path. AuNP probes

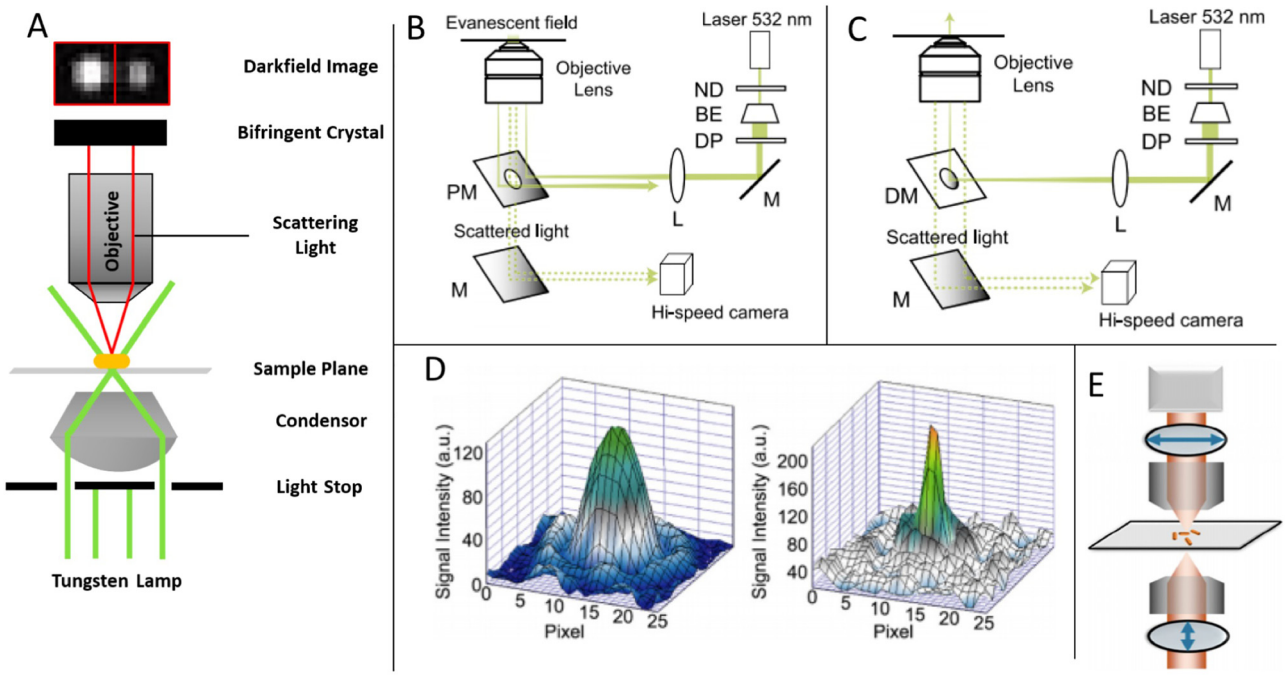

Fig. 3. (A) The working principle of dark field (DF) microscopy. Printed with permission from Iowa State University [57]. (B) Schematic illustrations of objective-type total internal reflection dark-field microscopy (TIRDFM) with a perforated mirror (PM) and (C) vertical illumination dark-field microscopy (VIDFM) with a dot mirror (DM). (ND) neutral density filter, (BE) laser beam expander, (DP) diaphragm, (M) mirror, (L) lens. (D) Intensity profiles of 40-nm gold nanoparticles by TIRDFM (left) and VIDFM (right). Pixel size = 88.5 nm. The profile was fitted by 2D-Gaussian. FWHM of PSF were 672 ± 36 and 623 ± 41 nm (n = 15), and 259 ± 48 and 212 ± 34 nm (n = 15) in the x- and y directions, for TIRDFM and VIDFM, respectively. Values are means ± SD. B–D are printed with permission from Elsevier [54]. (E) Setup for orientation-dependent localization microscopy (ODLM) for background free 3D imaging. Printed with permission from Springer Nature [56].

generate high contrast in the SPR wavelength channel, while the non-SPR wavelength channel that "turns off" the AuNP probes, is used as a control (Fig. 4B).

The use of full NA objective and condenser affords the shallower depth of field and thus better achievable axial (z) resolution than the conventional bright field and DF microscopes for optical sectioning of the samples. It was proven to provide good resolution both laterally and vertically for 3D imaging, which can be conveniently realized with a vertical scan of the focal plane through the specimen to acquire a series of z-stacked images and 3D image reconstructions using software [58]. When combined with AuNP imaging, full NA objective and condenser can be used to characterize the 3D localization and distribution of AuNPs as well as the aggregations of the AuNPs within cells [31,64,65]. For example, when the efficiency of different nuclear localization peptides that aid in the nuclear uptake of AuNPs was tested, video-enhanced color DIC microscopy allowed for localization of nanoparticles within HeLa and HepG2 cells [31]. Chithrani et al. used the combination of DIC and confocal microscopes to measure the uptake of transferrin-coated AuNPs into cells, where DIC was used to determine the z-positions of the nanoparticles [64]. Similarly, we utilized the optical sectioning ability of DIC microscopy to determine the subcellular location of nuclear targeting AuNPs, which were shown to be trapped and congregated at the outer nuclear membrane (Fig. 4C–F) [65].

Improving localization, precision, and resolution

It is important to obtain positions of the targeted single nanoparticle probes with high localization accuracy and precision in order to resolve the dynamic motions and interactions. Yet, the intrinsic diffraction limit of light prevents DIC microscopy from resolving nanoparticles that are separated by less than roughly half of the wavelength. The asymmetric point spread functions (PSF) further complicated the localization in DIC microscopy as they cannot fit into a simple mathematical equation like the common localization strategies used in other imaging techniques [66]. Despite such limitations, recent advancements in both instrumentation and methodology allow researchers to achieve improved resolution and localization of AuNPs in DIC microscopy [66–68]. Chen et al. reported the use of a structured illumination DIC (SI-DIC) microscope in the attempt of increasing the lateral resolution of DIC microscopy [67]. A lateral resolution of approximately 190 nm, a value that is double the wavelength found in conventional DIC microscopy, was achieved in the imaging of 53 nm polystyrene beads. This method can be adopted for sub-diffraction-limited imaging of AuNPs. Gu et al. reported a model-based correlation mapping method for precise 3D localization of spherical AuNPs and successfully applied the technique to localize 40 nm AuNPs inside fixed HeLa cells as well as to track the AuNPs in live A549 cells [68]. However, the model-based correlation mapping method does not work well for the localization of AuNRs as the DIC image pattern changes with respect to the orientation of the AuNRs. Different methods have been developed to solve this dilemma [66,69,70]. A dual-channel imaging system was developed by Gu et al. to localize AuNRs in the bright-field channel using transverse SPR with high accuracy as well as to track the rotational motions of the AuNRs in the DIC channel at the longitudinal SPR wavelength [69]. Zhao et al. presented a new localization strategy by combining computer simulated DIC images with the experimentally measured lateral shear distance in order to improve the localization accuracy of AuNRs [66].

Additionally, DIC microscopy has been used to study the interactions between nanoparticles and biomolecules using plasmon resonance energy transfer (PRET) to reveal cellular process within live HeLa cells [71]. This technique relies on the energy transfer from AuNPs to cytochrome c, a cellular protein involved in several signal transduction pathways, the most notable being the apoptosis signaling pathway. It is quantified by dips in the inten-

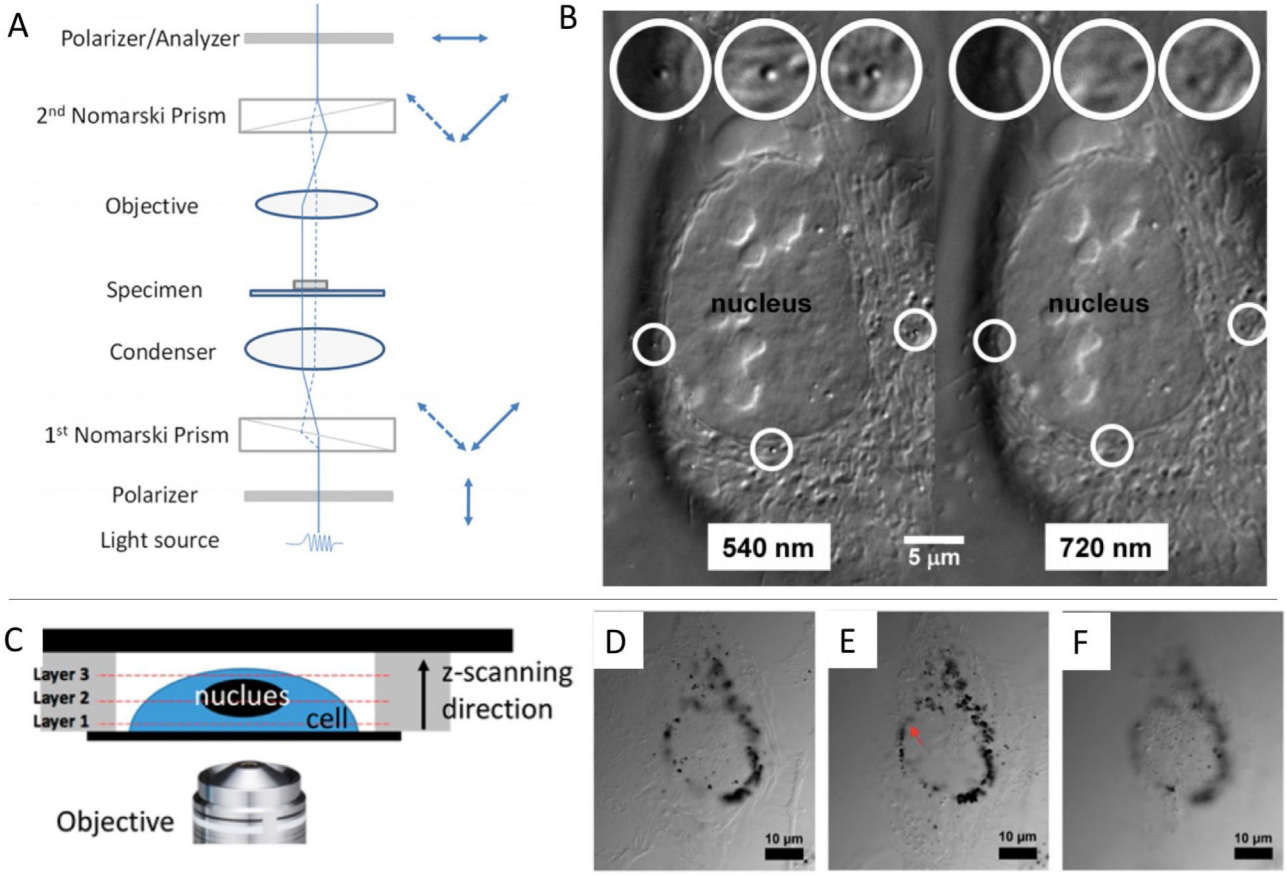

Fig. 4. (A) Differential interference contrast (DIC) microscopy working principle. Printed with permission from American Chemical Society [62]. (B) AuNP probes "turn on" in the surface plasmon resonance (SPR) wavelength channel (540 nm), while they "turn off" in the non-SPR wavelength channel in HeLa cells. Printed with permission from American Chemical Society [63]. (C) Scheme of optical section for nucleus targeted AuNPs' 3 dimensional cellular distribution, in ovarian cancer cell HEY A8. (D–F) the DIC images from layer 1–3 in C. Printed with permission from American Chemical Society [65].

sity of nanoparticle emissions that are measured by the change in the AuNPs' DIC contrast upon the interaction with endogenic cytochrome c protein during ethanol-induced apoptosis.

Other techniques for visualizing AuNPs

Interferometric scattering (iSCAT) microscopy

iSCAT is another label-free imaging method for visualizing AuNPs with high spatial resolution and sensitivity. In iSCAT microscopy, the samples are illuminated, and the reflected and scattered lights are collected and interfere at the detector [72]. It is composed of three main parts: (1) reflected light, (2) scattered light, and (3) the interference of the reflected and scattered light [73]. iSCAT collects the scattered light, which is the main signal in a DF image. Different from the DF microscope, the iSCAT has dominated reflected light that is avoided, however, in DF microscopy. The instrumentation set up and the operating principle are shown in Fig. 5A and B. An iSCAT image of a 30 nm AuNP moving along the microtubule is shown in Fig. 5C [74].

Using AuNPs as probes, iSCAT is applicable in resolving protein conformational changes down to **2 nm with millisecond temporal resolution** [74]. By attaching an AuNP as small as 20–30 nm on targeted motor proteins (such as myosin-5, kinesin-1, and dynein as examples), iSCAT was able to directly observe the structural transitions and protein dynamics [75]. High-resolution tracking of kinesin-1hydrolysis cycle showed that it uses a two[-step power-stroke mechanism [74]. In addition, Hancock group reported direct observation of the binding of individual tubulin dimers to growing microtubules [76]. iSCAT is also used for studying the behavior of lipids. Hsieh et al. achieved 1.9 nm spatial precision at 1 ms temporal resolution for tracking single particles on supported lipid membranes [77]. To resolve the dynamic molecular interaction between lipid rafts at the nanoscale, iSCAT is employed to record the motion of individual lipids and uses AuNPs as labels [78].

Photothermal imaging

For many of the existing imaging methods that based on AuNPs' Rayleigh scattering, their signal needs to be differentiated from the background. In practice, the minimum size of AuNPs is well above 30–40 nm. Consequently, the detection of smaller AuNPs is challenging. However, for smaller AuNPs, their strong absorbance could be converted to heat that warms up the environment surrounding the AuNPs. The temperature change of the medium will result in a reflection index change that shifts the phase of a transmitted light beam. By using this "photothermal" imaging, **we can see the AuNPs scale down to 1̃ nm in size** [79]. As shown in Fig. 6A, a green heating laser is focused on the sample and is absorbed by AuNPs as it generates a heat wave. The other red laser is split by a Wollaston prism into two orthogonally polarized beams, one of which coincides with the heating spot of the green laser. The two beams are recombined and the relative phase difference can be identified by the detector. The photothermal imaging is capable of differentiating very small Au nanospheres, which are nearly invisible in DIC microscopy (Fig. 6B–D) [80]. Recently, Zharov et al. demonstrated a

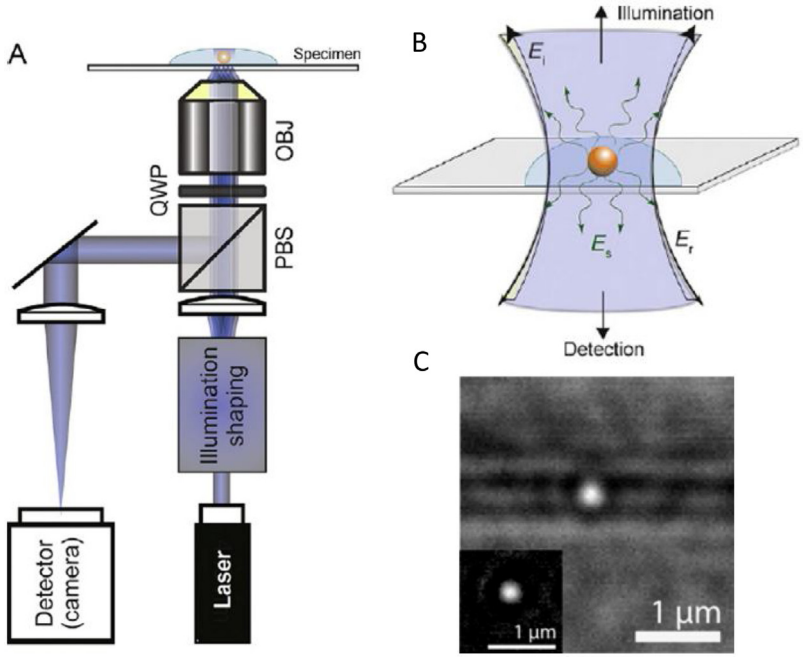

Fig. 5. (A) Optical setup for interferometric scattering (iSCAT) microscopy. OBJ: microscope objective; PBS: polarizing beam splitter; QWP: quarter-wave plate. (B) Operating principle of iSCAT. E_i is incident electric field; E_s is scattered electric field; E_r is reflected electric field. A and B are printed with permission from Elsevier [75]. (C) Raw iSCAT image of a 30 nm AuNP walking along a microtubule. (Inset) The image after background subtraction. Printed with permission from National Academy of Sciences [74].

super-resolution photothermal microscopy utilizing the non-linear dependence of signal on laser energy, with spatial resolution down to 50 nm [79].

Imaging rotational motion of gold nanoparticles

DIC microscopy for single particle orientation and rotational tracking (SPORT)

Birefringence, a phenomenon of orientation-dependent differences in the refractive index experienced by a transmitted wave through a specimen, is an intrinsic optical property in many biological materials. It was once considered a major disadvantage of DIC microscopy when compared to phase contrast microscopy. However, the birefringent gold nanorods (AuNRs) were well-explored as rotational imaging probes by Fang and co-workers to develop the DIC microscopy-based single particle orientation and rotational tracking (SPORT) technique in live cell imaging (a scheme is shown in Fig. 7A) [81]. It has transformed DIC microscopy into a primary single particle tracking tool to study the dynamic interactions of nanoparticles and cells, such as probing cellular membrane process, cellular uptake, and intracellular transport. The rotational information from AuNRs in highly dynamic cellular environments was extracted to correlate with bio-nano interactions and elucidate the underlying working mechanisms. Through visualizing the rotational patterns of AuNR probes, it was found that the surface properties of AuNRs could greatly influence their interactions with cell membranes, thus change the fate of these nanoparticles as drug delivery vectors [30]. AuNRs were also used to track the active transport events and pauses of endocytic vesicles movements along the length of an axon [82]. The ability to report the rotational motions during pauses in axonal transport is unattainable by other means. A fast imaging rate (500 fps) was used to visualize the unprecedented details on how kinesin and dynein motors transport endocytic cargos. Nanoparticles with different shapes, compositions, *etc.,* have been explored as SPORT probes. Micrometer long gold nanowires [83], multishell hybrid nanorods [84,85], gold nanourchins [86], and gold bipyramids [87] *etc* have been successfully characterized using DIC microscopy.

Although DIC microscopy can provide valuable information about the translational and rotational motions of the targeted AuNPs upon their interaction with biological surroundings, lack of molecular specificity is one of the major drawbacks. In order to differentiate the specifically-bind AuNRs with the non-specific ones, DIC based dual modality SPORT technique was employed to image and localize the docking and undocking of single AuNR-containing cargos (DIC imaging) on fluorescently-labeled microtubule tracks (fluorescence imaging) [88]. A recent study introduced by Chen et al. demonstrated an automated five-dimensional single particle tracking (x, y, z coordinates, azimuthal and elevation angles) of AuNRs in live cells with high accuracy (Fig. 7B and C) [70]. This method utilized the principle of parallax microscopy for spatial tracking and integrated DIC microscopy for rotational tracking. Mirror parallax-DIC images of AuNRs were used with a redesigned correlation mapping method for localization. Characteristic rotational motions of the transferrin conjugated AuNRs going through clathrin-mediated endocytosis and subsequent intracellular transport were visualized and recorded automatically. In addition, polarization modulation of the orientation-dependent AuNRs signal was used to superlocalize AuNRs even in aggregates with high lateral and axial resolution in single cells. To improve the resolution of rotational tracking, Chakkarapani et al. reported a method that combines integrated light sheet super-resolution microscopy (iLSRM) and DIC microscopy for resolving individual AuNRs in aggregated regions (Fig. 7D) [89]. Coupling DIC with other imaging techniques will definately be a trend in future development. Integrated DIC microscopy will be able to provide more comprehensive molecular and structural information of the biological systems and will help to decifer more complex interactions of nanoparticles and biological surroundings in dynamic cellular processes.

Dark field microscopy for rotational tracking

The first reports of rotational tracking with plasmonic nanoparticles visualized the 2D rotation of the AuNRs attached to a glass

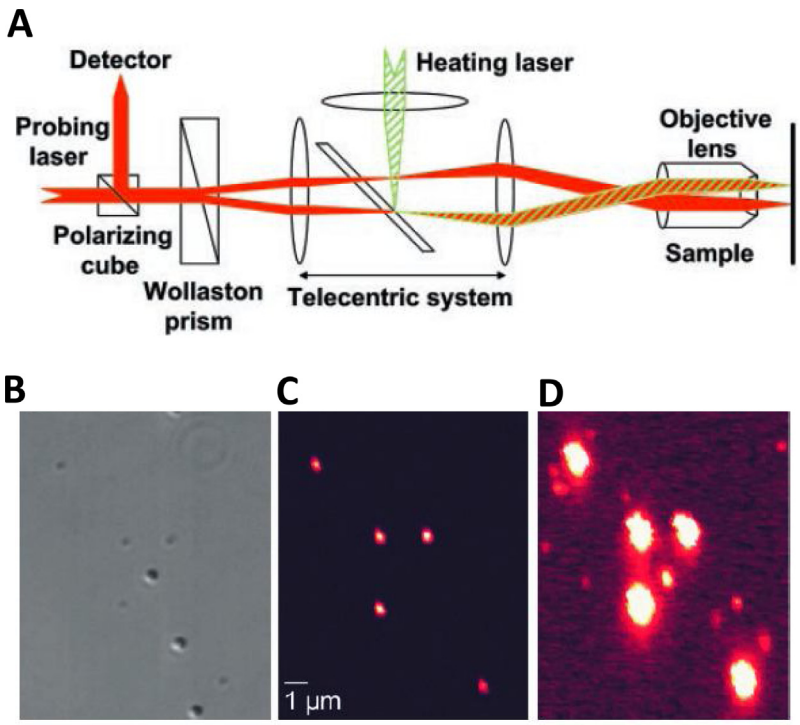

Fig. 6. (A) Optical setup of photothermal optical microscope. (B) Differential interference contrast (DIC) imaging and (C–D) photothermal images of a sample containing 300 nm latex spheres, 80 nm Au nanospheres, and 10 nm Au nanospheres. DIC image shows the 80 nm Au nanospheres and 300 nm latex spheres, while the 10 nm Au nanospheres are invisible. (C) The photothermal image with lower laser heating intensity showing the 80 nm Au nanospheres. (D) The photothermal image with higher laser heating intensity enables clear visualization of 10 nm Au nanospheres with 80 nm AuNPs reaching saturated detection. Printed with permission from American Association for the Advancement of Science [80].

surface [90] or single F1-ATPase molecules [91] using polarized light scattering in DF microscopy. The scattered light from each AuNR was split by a birefringent crystal into two orthogonal polarization channels, generating two spots that were imaged simultaneously [90]. The orientation-dependent scattering intensity is proportional to $(\cos(\theta))^2$, where θ is defined as the angle between the long axis of the AuNR and the polarization direction. Dual-channel DF microscopy was also used to investigate the AuNR dynamics in cellular internalization processes [92].

Xiao et al. deployed a defocused DF imaging technique to determine the 3D orientation of AuNRs through deconvolution of the field distribution pattern in defocused DF images [93]. 3D orientation of AuNRs was resolved without degeneracy by using pattern recognition. Enoki et al. developed objective-type vertical illumination DF microscopy using a reflected dot mirror. Both dual polarization and defocused imaging methods were applied and compared in the study on the rotation of the rotary molecular motor, F1-ATPase, with microsecond temporal and one-degree angle resolution [94]. Recently, Cui et al. demonstrated the use of multi-polarization DF imaging for orientation determination of endosomes during the axonal transport to gain insight on the working mechanisms of motor proteins [95,96].

In order to overcome the angular degeneracy, total internal reflection scattering (TIRS) microscopy was used to determine the full 360-degree orientation of AuNRs [97]. Focused orientation and position imaging (FOPI), a TIRS method reported by Ha et al. utilized the coupling between the AuNRs and gold film using a linearly-polarized laser to generate characteristic donut-shaped PSF patterns for full 360-degree orientation determination [97].

Other nanoparticle-based rotational tracking techniques

AuNRs are ideal orientation probes for photothermal imaging as the intensity can be modulated through the change in polarization. Chang et al. utilized the polarization-sensitive photothermal imaging technique to image of the orientation of AuNRs, and, consequently, verified the orientation measurement of the same AuNRs with correlated with SEM [98]. Thus, quantitative orientation angles of AuNRs were obtained from the photothermal polarization traces. Zhang et al. demonstrated the imaging of orientation and dichroism of non-spherical nanoparticles using polarization modulation thermal lens microscopy as an alternative method to fluorescent techniques [99].

Adopted from fluorescence correlation spectroscopy (FCS), correlation spectroscopy methods have been developed to characterize the rotational and translational dynamics of AuNRs [100,101]. Similar to FCS, it relies on the principle of correlation analysis of the time-dependent intensity fluctuation to obtain quantitative information. One-photon luminescence correlation spectroscopy was reported in a study of measuring the hydrodynamic sizes and investigating the rotational and translational dynamics of AuNRs [100]. The intrinsic luminescence signals emitted by surface plasmon were detected, and fast interconversions between hot electron-hole pairs and surface plasmons were investigated. Zhang et al. reported a sensitive resonance light scattering correlation spectroscopy method for characterizing rapid rotational and translational diffusion of AuNRs in solution [101]. Translational and rotational diffusion coefficients, as well as aspect ratios of AuNRs, were obtained from wavelength-dependent resonance light scattering fluctuations within a focused observation volume. Detection of DNA hybridization and the homogeneous immunoassay were demonstrated.

Janus particles are another group of rotational probes. They are typically fabricated from metal coating that constitutes one half and fluorescent molecules that make up the other half. Kopelman et al. introduced a type of optical anisotropic Janus particles named modulated optical nanoprobes (MOONs) as rotational probes [102].

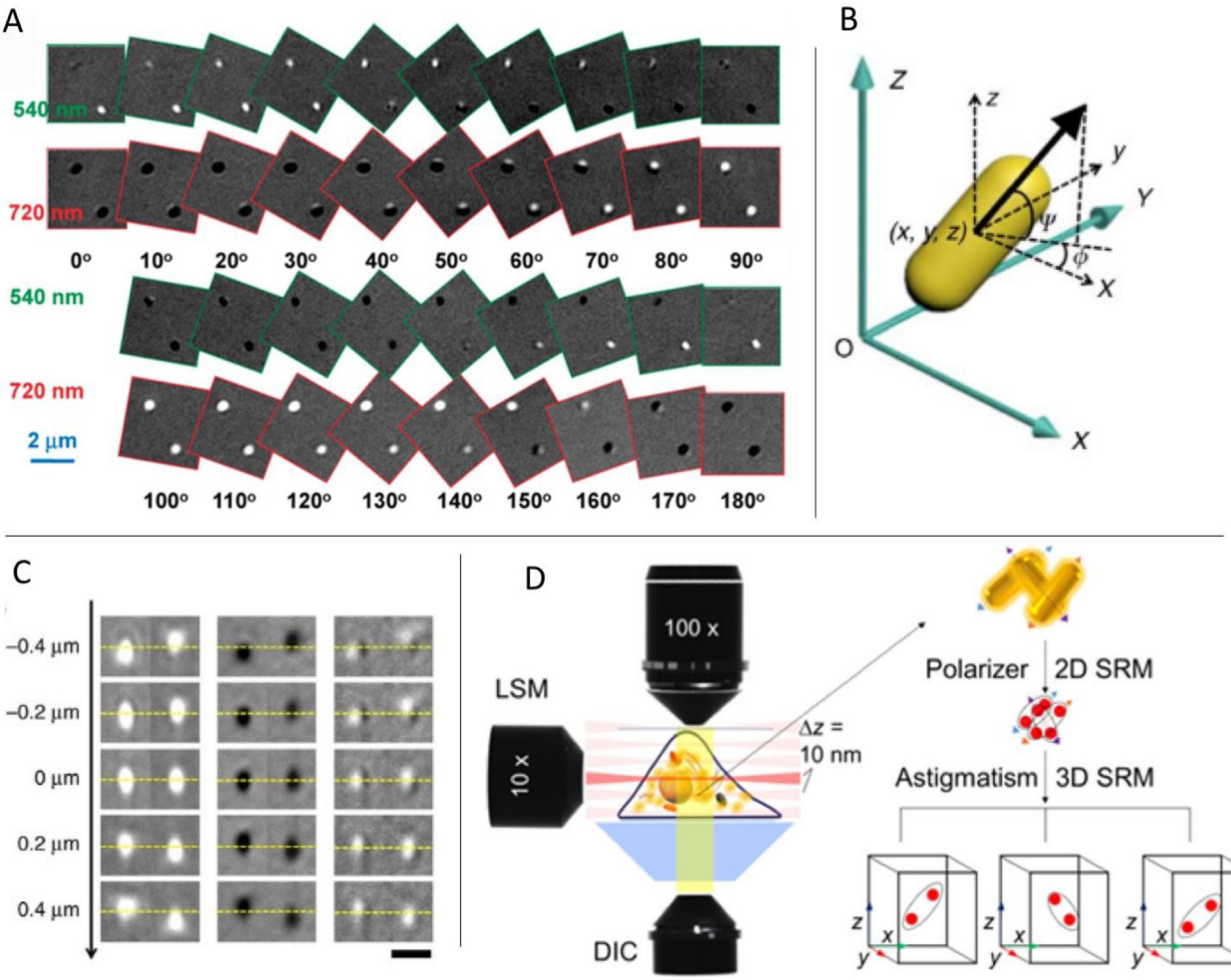

Fig. 7. (A) DIC images of two immobilized AuNRs (25 × 73 nm) adsorbed on glass slide collected under the illumination of 540 nm and 720 nm (transverse and longitudinal plasmonic resonance wavelengths) on a rotating stage. Printed with permission from American Chemical Society [81]. (B) Schematic drawing of a AuNR placed in the 3D coordinate system. The x- and y-axes are set according to the polarization directions of the illumination light. The dipole shown here corresponds to the long axis of the AuNR, whose centroid locates at (x, y, z). The azimuthal angle and the elevation angle of the longitudinal axis of the AuNR are presented as ϕ and ψ, respectively. (C) Bright (left), dark (middle), and half-bright/half-dark (right) images of a gold nanorod (40 nm × 80 nm) at different orientations and vertical positions. The half-plane images are aligned by the nanorod's center of mass at the focal plane (z = 0 μm). The yellow dashed lines indicate the z position of the center of the gold nanorod in focus. Scale bar is 1 μm. B and C are printed with permission from Springer Nature [70]. (D) The combination of differential interference contrast (DIC) and light sheet microscopy (LSM) for tracking 3D orientation of anisotropic AuNRs. Printed with permission from American Chemical Society [89].

The orientation of the MOONs can be remotely controlled using a magnetic field and the modulation of fluorescence intensity was used to correlate to local interactions. Janus particles of different shapes and morphologies have been explored as rotational probes in biological imaging and sensing [103,104]. Gao et al. reported the rotational tracking study of micrometer-sized single-Janus rods with different fluorescent colors on two sides in live cell [105].

Recently, Lee et al. designed a polarization selective iSCAT (psiSCAT), enabling the capture of rotational as well as positional information on particles [106]. psiSCAT enables the rotational tracking ability with high spatial resolution.

Molecular fingerprinting by surface-enhanced Raman scattering (SERS)

Compared with other imaging techniques, SERS can provide highly sensitive and abundant structural information (Fig. 8A). SERS can detect biomolecules of interest that surround the nanoparticles by a factor of over 10 orders of magnitude compared to normal Raman signals [25]. Furthermore, SERS signals increase in sensitivity when the distance between the Raman reporters and the AuNPs decreases – the shorter the distance, the stronger the SERS signal [107], making it ideal for studying bio-nano interactions. The powerful targeting of nanoparticles through ligand conjugation creates high specificity on their locations. In addition, the range of accessible wavelengths for SERS detection extends from the whole visible spectrum to NIR [108], the latter accounting for the maximum penetration depth within biological samples.

Single molecule SERS

Ultrasensitive detection at extremely low concentrations (femto- or attomole) is limited by diffusion; therefore, the time needed to find and detect a molecule could be unrealistically long. To solve this problem, de Angelis and co-workers developed a method that combines super-hydrophobic artificial surfaces and nanoplasmonic structures to detect a few molecules (10^{-18} mol L^{-1}). By loading a drop of solution that contains the molecules onto a super-hydrophobic surface (periodical silicon micropillar arrays with plasmonic nanostructures on the top of the pillars), the droplet gradually evaporates to increase the concentration of the molecules inside and shorten the detection time with SERS

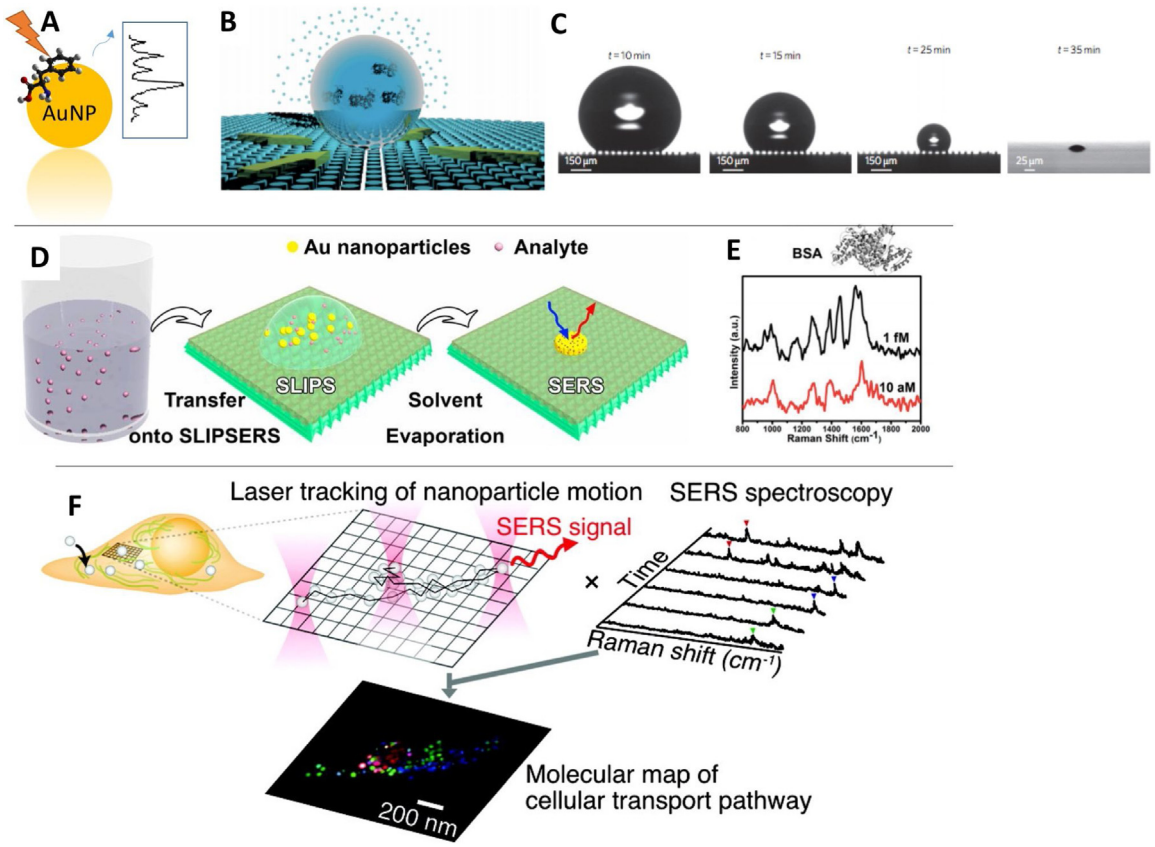

Fig. 8. (A) Principle of surface-enhanced Raman scattering (SERS). (B) Sing-molecule detection by super-hydrophobic surface (periodical silicon micropillar arrays with plasmonic nanostructures on the top of the pillars). (C) The optical images of the analyte drop on the micropillar arrays evaporating at four different times. The B and C are Printed with permission from Springer Nature [109]. (D) Single-molecule detection platform named slippery liquid infused porous surface-enhanced Raman scattering (SLIPSERS). (E) Ultra-sensitive detection of BSA protein using the platform of D. D and E are printed with permission from National Academy of Sciences [110]. (F) SERS spectra changes during AuNP endocytosis. Printed with permission from American Chemical Society [113].

or surface-enhanced fluorescence (Fig. 8B and C) [109]. A similar but more practical strategy has been reported by Yang et al. for the quantitative detection of rhodamine 6 G (R6 G) down to 10^{-15} mol·L^{-1} using a platform named slippery liquid infused porous surface-enhanced Raman scattering (SLIPSERS), in which a drop of the analytes and SERS substrates (*e.g.*, AuNPs) were added onto a slippery surface, and the resulting evaporation of the liquid droplet allows for nearly 100% analyte collection efficiency (Fig. 8D and E) [110].

DNA origami has been recently utilized for directed formation of Au nanostructure for single-molecule SERS due to its ability to exert precise control over the geometrical configuration such as fabricating the Au nanodimers with a hot spot. Sen et al. prepared Au nanostar dimers on dimerized rectangular origami structures, with 7 and 13 nm interparticle gaps and achieved 2×10^{10} and 8×10^{9} enhancement, respectively [111]. Ding's group constructed 80 nm plasmonic bowtie nanostructures *via* a DNA origami-based bottom-up assembly strategy that have an approximate 5 nm gap and obtain SERS enhancement about 10^{9} [112]. The DNA origami technique is very promising for revolutionizing the SERS detection, providing accurate fabrication methods for SERS probes with a high degree of customization.

SERS in studying the bio-nano interaction

Researchers have tracked the nanoparticle motion inside living cells and have provided the molecular maps of organelle transport and liposomal accumulation of the AuNPs, indicating the different types of transport pathways [113,114]. The SERS spectra changes in space and time during AuNP endocytosis provide the change in the cellular environment (Fig. 8F). Consequently, the SERS spectra provide molecular maps dynamics during organelle transport and lysosomal accumulation of AuNP [113]. In addition, SERS was used to monitor the real-time photothermal ablation of cancer cells, for "seeing-and-treating". When exposed to light, AuNPs can convert light energy to heat, which can be used to kill cancer cells (otherwise known as the photothermal effect). Ali et al. used SERS to study the molecular mechanism of AuNR-assisted photothermal ablation and observed an increase in specific Raman bands during the process [115]. A similar method for SERS-guided photothermal therapy has been used by Sun et al. [116]. In addition, SERS has also been employed to image and explore the biosynthetic mechanism of AuNPs. As shown in the study by Lahr et al. the intracellular and extracellular AuNP biosynthesis process by green algae was revealed by SERS by identifying the surface-associated biomolecules. The SERS peaks indicate the participation of identified molecules in elucidating the mechanism of the biosynthetic process [117].

In vivo *SERS imaging for tumor diagnosis and therapy*

In 2008, one of the pioneer studies demonstrated the ability to collect the SERS spectra from tumor-bearing mice that were injected with AuNP probes [118]. Recently, several studies reported the use of SERS on tumor detection and imaging. SERS has been well applied to *ex vivo* analysis of tissue slides. It could assist in cancer surgery to ensure complete removal of tumors, with fast speed and high sensitivity. Wang et al. developed probes that targeted

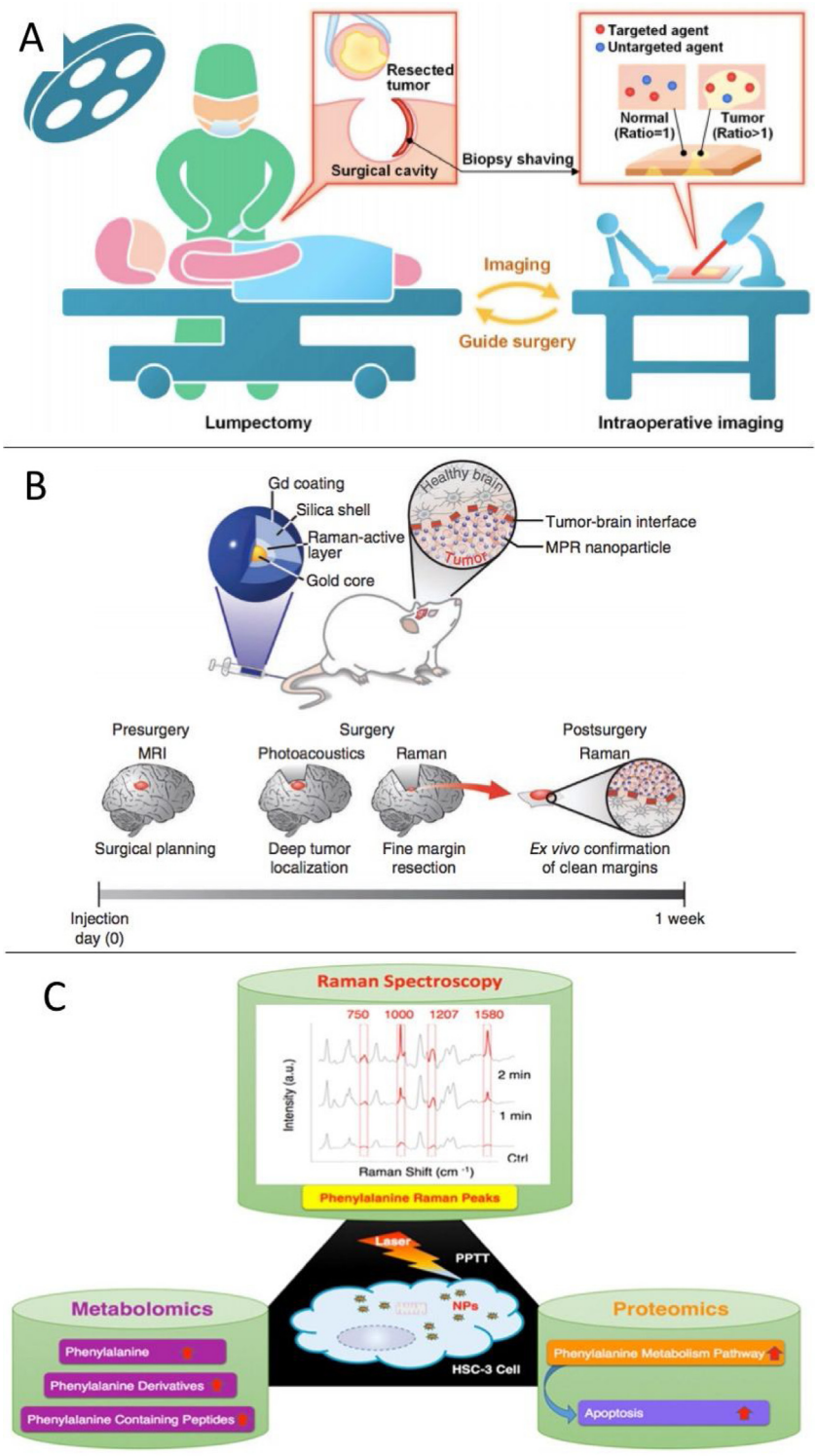

Fig. 9. (A) Surface-enhanced Raman scattering (SERS) aids cancer surgery. Printed with permission from Springer Nature [119]. (B) Schematic of SERS probes for confirming the brain tumor margins. Printed with permission from Springer Nature [121]. (C) SERS and mass spectrometry-based proteomics and metabolomics for understanding the cell death mechanism after plasmonic photothermal therapy. Printed with permission from American Chemical Society [115].

and visualized a multiplexed panel of cancer biomarkers. The AuNP probes were then put onto freshly excised tissues to determine the presence of cancer cells. This technique could achieve in fast detection (less than 15 min) for potential intraoperative use in guiding breast-conserving surgeries (Fig. 9A) [119]. A dual probe approach that consists of two types of SERS probes (one EGFR-specific and one non-specific) was applied to fresh tissue for measuring the EGFR concentration with the subtraction of the background signal [120]. Kircher et al. showed a triple-modality magnetic resonance imaging (MRI)–photoacoustic imaging–Raman imaging (MPR) nanoparticle (Fig. 9B), where SERS was used to accurately delineate the margins of brain tumors in living mice due to its ultrahigh sensitivity and spatial resolution. Raman imaging allowed clear signal from particles down to 50 pM, which is very low for *in vivo* imaging [121].

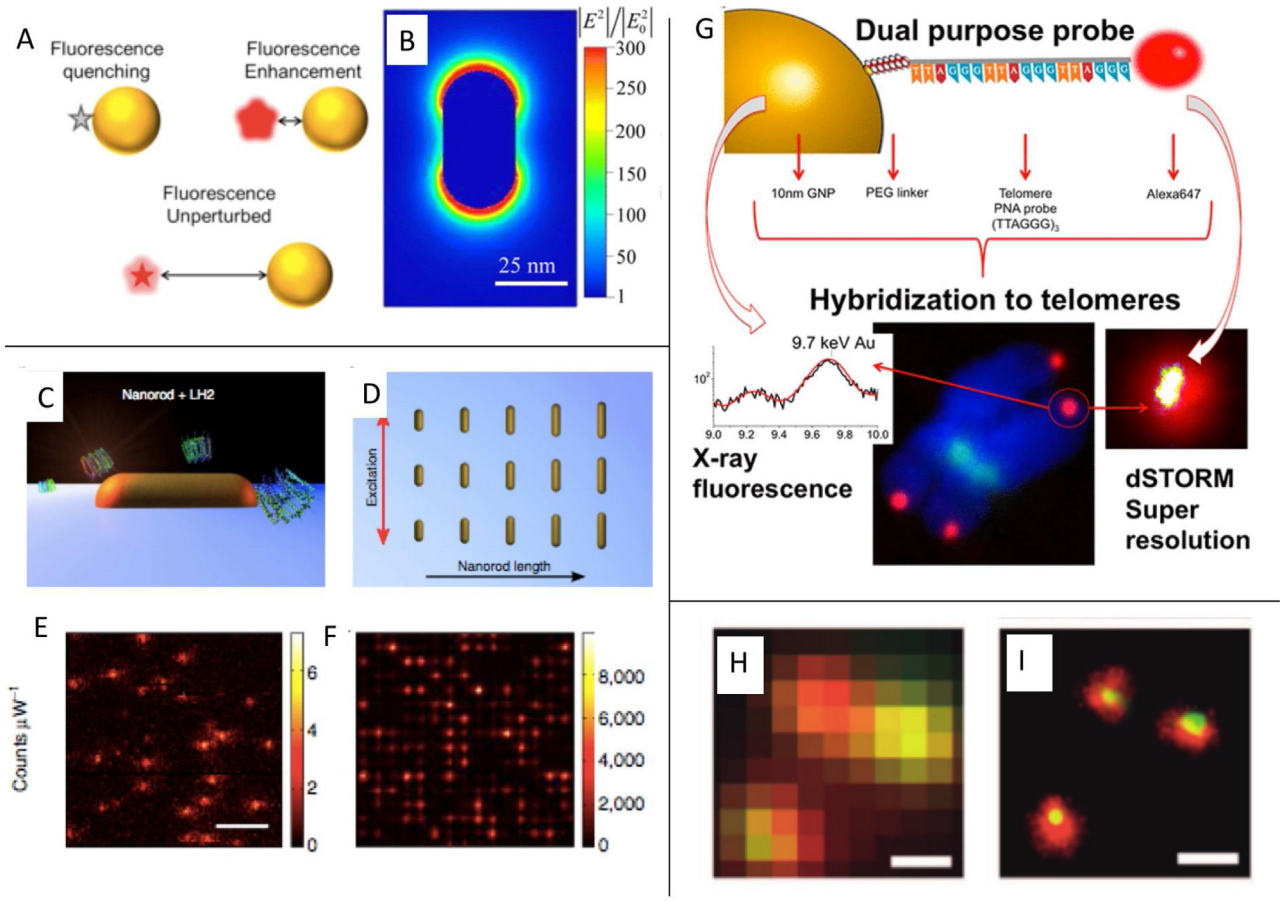

Fig. 10. (A) Plasmon-enhanced fluorescence (PEF) working principle. Printed with permission from American Chemical Society [129]. (B) PEF of individual AuNR for single molecule detection. Printed with permission from American Chemical Society [136]. (C–F) AuNR arrays for studying the light harvesting complex 2 protein. C shows the schematic of an AuNR with an LH2 complex at the hot spot. D is a schematic figure of the AuNRs array. E and F are Fluorescence images of LH2 complexes on the surface of PVA (E, without AuNRs) and on the surface of AuNR arrays (F). Printed with permission from Springer Nature [137]. (G) AuNPs with DNA points accumulation for imaging in nanoscale topography (DNA-PAINT) for determining the telomeres distance. Printed with permission from American Chemical Society [144]. (H–I) the difference in resolution of (H) a wide-field and (I) a STORM image for protein corona. Scale bar: 200 nm. Printed with permission from John Wiley and Sons [146].

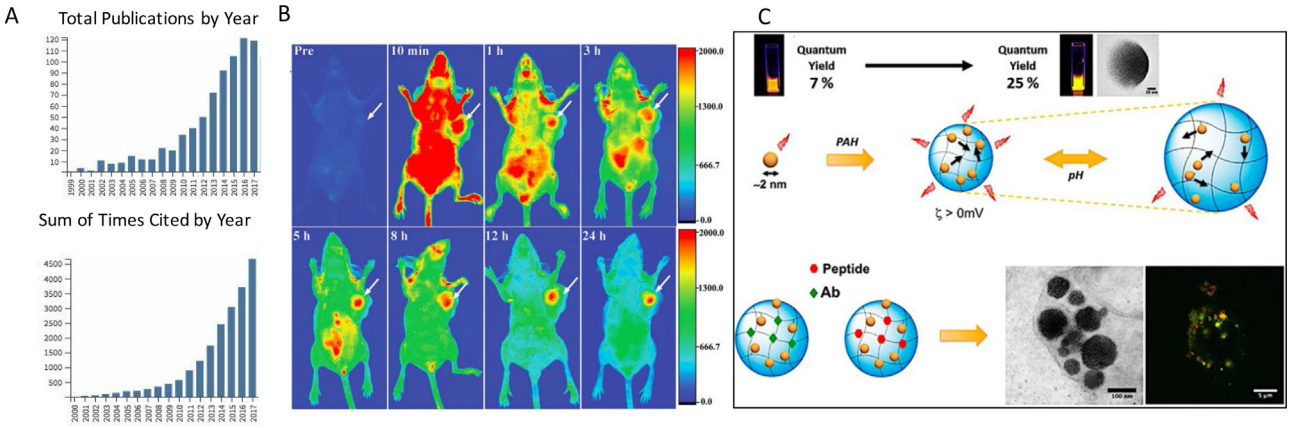

Fig. 11. (A) The publications and citations of the gold nanoclusters (AuNCs) in bioimaging (from Web of Science search "gold nanoclusters" and "imaging"). (B) Fluorescence imaging of tumor sites in mice (MGC-8) and the biodistribution and excretion pathway of the AuNCs (0–24 h post injection times). Printed with permission from John Wiley and Sons [160]. (C) Polymer mediated AuNC self-assembly into pH-dependent nanoparticles of *ca.* 120 nm diameter enhanced the fluorescence intensity in human monocytic cells. PAH, poly(allylamine hydrochloride); Ab, antibody. Printed with permission from American Chemical Society [163].

Although working well in glioblastoma mouse models, this method has not been very successful in other extracranial tumor models, a result possibly due to the lower enhanced permeability and retention EPR effect, as mentioned by the one of the group's recent paper [122].

Recent improvements of gold nanoparticle-based SERS

Although the SERS probes have high sensitivity, the Raman intensity is greatly attenuated as it travels through tissue due to scattering. To increase the tissue penetration, a combination of

the deep Raman spectroscopy with surface-enhanced, spatially offset Raman spectroscopy (SESORS) was developed and greatly improved the penetration depth from less than 5.5 mm to 25 mm thickness [123]. As mentioned earlier, the Raman reporter in the NIR range could reduce the tissue scattering greatly. Gold nanostructures such as AuNRs could assist in this purpose. Maltzahn et al. used nanorods coated with SERS active molecules that could be uniquely distinguished *in vivo,* over a spectral sharp bandwidth of 6 nm in the NIR (is much smaller than that of semiconductor quantum dots (QDs) (~30 nm FWHM), organic fluorochromes, and Raleigh scattering nanoparticles). This platform has been used for both SERS imaging and plasmonic photothermal therapy in mice [124]. Qian et al. used functionalized AuNRs (conjugated with Raman markers), for sentinel lymph node (SLN) mapping and tumor targeting of mice, as well as for the observation of the distribution and excretion of intravenously injected AuNRs in deep tissues through purely optical imaging *in vivo* [125].

To improve the SERS probes for high-sensitive bioimaging, bi-layered Raman-intense gold nanostructures with hidden tags (BRIGHTs) were developed. The Raman reporters are trapped between the core and shell of the gold nanostructures. This design exhibited great stability and demonstrated more than two orders of magnitude in the enhancement of the SERS signal compared with conventional AuNP SERS probes [127]. Another big obstacle for using SERS as an imaging tool is its limitation on resolution and speed. Kang et al. developed a method to achieve high-speed and high-resolution live cell SERS imaging, using NIR excitation (785 nm) and high-speed galvano mirror-equipped confocal Raman microscopy system. This system leads to accomplish the high resolution (50×50 pixels) single live cell imaging within 30 s (10 ms/pixel) and with subcellular resolution of cytoplasm, mitochondria, and nucleus [126]. The SERS-sensitive AuNPs have a highly narrow intra-nanogap (1.2 nm) and Raman markers embedded, allowing for high-sensitive imaging.

In addition, SERS presents its own problems for spectroscopy, such as the complex and overlapping Raman bands that are sometimes difficult to understand. In many cases, the SERS bands are a mixture of all types of molecules in the environment of AuNPs. The method used in El-Sayed's lab utilized mass spectrometry along with SERS to improve the understanding of the cellular process in plasmonic photothermal therapy (PPTT). By using metabolomics and proteomics, the changes in SERS bands can be assigned to specific chemical compounds within the cells with an improved degree of confidence (Fig. 9C) [115].

Gold nanoparticles in fluorescence imaging

The plasmon-enhanced fluorescence (PEF) was observed shortly after the discovery of SERS [128]. AuNPs have shown to greatly increase the excitation of fluorescence probes where the overlap between the SPR of AuNPs and the absorption and emission spectra of the fluorophore occurs [27]. The distance between the AuNP and the fluorophore affects the fluorescence intensity: fluorescence quenching within a very short separation distance (~2 nm), and enhancing when within an optimal separation distance (~5 nm), yet unchanged fluorescence when the separation distance is far (~20 nm) (Fig. 10A) [129]. The plasmonic properties of AuNPs enable us to study specimen with weak fluorescence emission, sometimes even at the single molecule level [130,131], and provides us with the opportunity to utilize high-resolution imaging in order to overcome the diffraction limit [129]. The production of PEF substrates have been summarized in a recent review article [27]. In this review we will focus on the recent biological applications. On the other hand, the fluorescence emitted from specific gold nanoclusters (AuNCs) can also be used for imaging with excellent anti-photobleaching properties even under strong light illumination [132]. Compared to similarly fluorescent quantum dots, AuNCs exhibit better bio-safety [133].

Single-molecule fluorescence detection

The detection of single biomolecules, especially in their native physiological conditions, is highly challenging. Gold nanoantennas with varied structures have been used to amplify the fluorescence signal to allow for single-molecule fluorescence detection. Due to the "hot spots" in enhancing the excitation field and the increased quantum efficiency, they function in a way similar to the traditional radio-wave antennas [134]. Moerner's lab used a gold bowtie nanoantenna to achieve large single-molecule fluorescence enhancements up to a factor of 1340 [135]. Khatua et al. examined the enhancement of single-molecule fluorescence from a weak emitter, crystal violet, by individual AuNRs (Fig. 10B). The fluorescence could be enhanced more than 1000-fold when the SPR of AuNRs was at 629 nm and excited at 633 nm [136]. Furthermore, Wientjes et al. designed AuNRs arrays that could obtain over 500-fold fluorescence enhancement of a protein (light harvesting complex 2, LH2) at the single-molecule level (Fig. 10C-F). Using this platform, they observed the photon antibunching from a single LH2 complex, which acts as a nonclassical single-photon emitter [137]. Akselrod et al. reported a silver nanocube situated on a gold film (separated by a 5–15 nm spacer layer, which contains fluorescent material) that obtained a PEF exceeding 1000 times [138]. In addition, a double nanohole aperture in a metal film has been used for single protein detection [139], acting as a volume confinement and fluorescence enhancement [140], as well as an optical tweezer with high-efficacy trapping ability [141]. Gold nanoantenna can also greatly enhance the Förster resonance energy transfer (FRET), where dipole-dipole exchange happens between a pair of donor and acceptor dipoles when they are separated by 1–10 nm in distance. As an example, Juan de Torres et al. fabricated a nanogap antenna that could enhance the FRET efficiency up to 50% for the nearly perpendicular donor and acceptor dipoles [142].

Super-resolution fluorescence imaging

AuNPs can be used to improve the spatial resolution of fluorescence imaging. Masuda et al. fabricated a 2D sheet of AuNPs to achieve enhanced fluorescence and used it to study the interactions between nanomaterials and biological components. Test cells with fluorescence-labeled actin filaments revealed that this method was able to achieve high axial and lateral resolution under a regular epi-fluorescence microscope [143]. In addition, AuNPs together with the DNA points accumulation for imaging in nanoscale topography (DNA-PAINT) technique enables the measurement of small structural distances inside cells. Due to the unprecedented spatial resolution of ~5 nm, DNA-PAINT super-resolution microscopy was used by Jeynes et al. to determine the nanometric properties of human telomeres. They made use of a compatible dual probe composed of AuNPs and fluorescent capabilities, by a way of combining direct stochastic optical reconstruction microscopy (dSTORM) imaging and X-ray fluorescence microscopy. This probe design was able to measure the absolute dimensions of individual telomeres in human cells (Fig. 10G) [144]. The DNA-PAINT technique also enables the super-resolution optical imaging of AuNRs. Recently, Taylor et al. determined the all-optical reconstruction of AuNRs geometry using super-resolution microscopy, with the DNA-PAINT technique, enabling the imaging of a single AuNR without the use of electron and atomic force microscopy. The reconstructed dimensions deviate by no more than ~10% in comparison to the actual size of the AuNRs. This method is benefi-

cial for the use in biological systems where access to electric beams or tip based probes is restricted [145].

With further emphasis on the impact of appropriate imaging techniques on the development of tailored therapies that involve nanoparticles, researchers employed dSTORM imaging to investigate the protein corona with single protein sensitivity (Fig. 10H-I). With this microscopy technique, the proteins that were adsorbed onto the surface of the particle were quantified and it was determined that the corona has a certain dynamic heterogeneity [146]. Although mesoporous silica nanoparticles were used in the methodology, it should be applicable to AuNPs, and plasmonic enhancement could be further utilized.

Fluorescence in studying bio-nano interactions

Fluorescence imaging has been used to examine the endocytic uptake process of AuNPs [147,148]. In addition, PEF has also aimed to guide photodynamic therapy (PDT). Huang et al. developed a photo-theranostic agent, chlorin e6, that was conjugated with silica-coated gold nanoclusters to guide in fluorescent imaging for PDT [149]. The platform has enhanced the cellular uptake of chlorin e6 and has good biocompatibility. The use of AuNRs enables NIR fluorescence, a more favorable range for *in vivo* purposes. As fluorescence can be manipulated by the distance between the AuNRs and the fluorophore, Jang et al. developed an AuNR photosensitizer in which the fluorescence emission (originally quenched as the fluorophores formed complex with AuNRs) was dequenched when the AuNRs were exposed in the tumor, as the fluorophores were released from the surface of the AuNRs [150]. Tumor sites were clearly visible in the NIR images after one hour. As AuNRs can act as photothermal generators, this design can also be used to visualize and treat tumors *in vivo*. In addition, Qian et al. functionalized AuNRs with both NIR fluorescence and SERS probes for *in vivo* optical imaging of the sentinel lymph node as well as tumor targeting in mice [125]. Owing to the strong fluorescence enhancement from the clustered AuNPs, Hayashi et al. developed clustered 7 nm AuNPs with fluorescent silica core-shell nanoparticles (the fluorophores covalently bind to silica) for the CT-fluorescence dual-mode imaging of tumors, which can be used before or during surgery [151].

Fluorescent gold nanoclusters (AuNCs)

It has been widely recognized that gold nanoclusters (AuNCs) display strong intrinsic fluorescence that highly photostable. Their application in bioimaging is relatively new and at the preliminary stage, but this area is growing very rapidly (Fig. 11A). AuNCs are essentially AuNPs that have a diameter shorter than 2–3 nm (usually composed of several to hundreds of gold atoms whose size is comparable to the Fermi wavelength of the electrons [152], and the continuous band breaks into discrete energy levels), and are too small to support the SPR effect, but they exhibit fluorescence in the visible or NIR regions [153,154]. Several synthetic strategies for preparing AuNCs that prevent them to agglomerate into large nanoparticles were reported. These strategies include the chemical reduction from gold ions followed by the capping of ligands such as thiols, peptides, or proteins as well as finally the direct etching from AuNPs [153,155]. Here we briefly introduce the recent advances in AuNCs imaging from 2014 until now.

Due to their intrinsic fluorescence, many studies have used AuNCs for the direct imaging of cells and animals. AuNCs allow for the directly imaging of their internalization process into cells. In the work of Venkatesh et al. green AuNCs capped with 8-mercapto-9-propyladenine were able to accumulate in the cell nuclei with high specificity [156]. Similar nuclear staining phenomena were also observed by Wang et al., where red AuNCs (680 nm) were stabilized by a tripeptide (Lys–Cys–Lys) [157]. Moreover, Fernandez et al. studied the effect of AuNCs (stabilized by different ligands) on human derived-monocyte dendritic cells regarding their different intracellular accumulation patterns and different immune responses [158].

Chandirasekar et al. reported biosurfactant (sodium cholate) templated green AuNCs, which were used in the *in vivo* imaging of zebrafish embryos. Their results indicated that AuNCs exhibited no significant toxicity in developing embryos up to 100 μL/mL and were stable in living organisms [159]. Zhang et al. displayed *in vivo* images of tumor sites in mice and studied the biodistribution and excretion pathway of the AuNCs in tumor-bearing nude mice. Their results revealed that AuNCs have superior penetration and retention in tumors (as shown in Fig. 11B) [160]. On the other hand, the *in situ*-synthesized AuNPs can also be used for imaging tumors. Wang et al. established a method where the chloroauric acid solutions were injected into mice tumors, and the spontaneously biosynthesized fluorescent gold nanoclusters could be used for detecting the tumor locations [161].

To obtain AuNC probes with better properties, several strategies have been developed. Zhao et al. fabricated a dual-emission fluorescent nanohybrid, constructed from far-red AuNCs and NIR PbS QDs (AuNCs-PbS-QDs). This nanoprobe exhibits two well-resolved emission peaks (640 and 813 nm) for built-in correction of the environmental interferences due to the large separation between the two peaks. The double peaks are more favorable for bioimaging. They demonstrated several applications of this probe by detecting ascorbic acid in a fruit internal quality assessment, *in vitro* cellular imaging, and *in vivo* imaging in nude mice [162]. In addition, Yahia-Ammar et al. reported a method using cationic polymer-mediated AuNCs that self-assemble into large particles with an overall size of 120 nm diameter, and they have pH-dependent swelling properties. The fluorescence of this platform was magnified more than 3-fold with low cytotoxicity (up to 500 μg Au/mL) (Fig. 11C) [163].

AuNPs assist *in vivo* optical imaging

For most of the optical microscopic techniques, the imaging depth for tissue samples is limited to several hundred μm. This is due to the strong scattering that greatly decreases the depth a photon can travel within the tissues. Recent advances enable deep tissue imaging, including non-linear optical imaging (such as two-photon microscopy), photoacoustic imaging (PA), optical coherence tomography (OCT), optical projection tomography, selective plane illumination microscopy, *etc.* [164]. The SPR of the AuNPs enables the enhancement of two/multi-photon absorption, and acts as a contrast agent that assists in photoacoustic and OCT imaging. Here we mainly focus on the recent advances of AuNPs in two/multi-photon imaging, PA and OCT techniques in deep tissue imaging *in vivo*.

Two-photon and/or multiphoton imaging

In two-photon imaging (TPI), two NIR (or longer wavelengths) photons are usually used to excite a fluorophore within a visible range (Fig. 12A). The use of NIR excitation light in TPI greatly minimizes the tissue background scattering, and improved imaging depth can be achieved, notable up to **several hundreds of micrometers or even on the millimeter level** compared to the depth from conventional fluorescence imaging [165]. TPI has found applications in high-resolution 3D imaging. As such, this imaging mechanism also greatly benefits from the use of AuNPs that resist photobleaching and exhibit the stable SPR needed for excitation by each photon. The SPR of AuNRs enables them to have a two-photon absorption coefficient 10–100 times larger than organic fluorophores [32,166]. Some early exploration has observed that

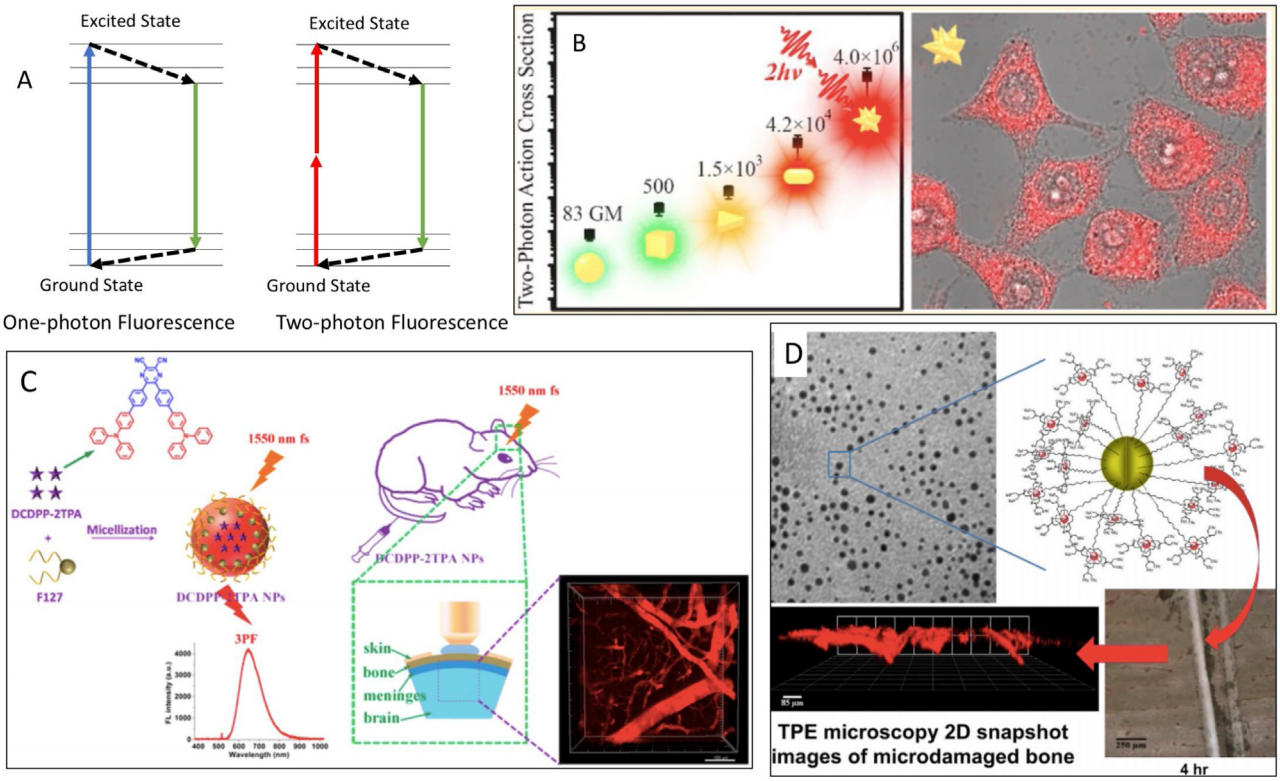

Fig. 12. (A) Two-photon imaging (TPI) working principle. (B) Difference enhancements from varied sizes of AuNPs. The right side contains gold nanostars for TPI in HepG2 cancer. Printed with permission from American Chemical Society [168]. (C) Aggregation-induced emission luminogen with a large three-photon absorption cross section *in vivo*. The DCDPP-2TPA NPs were synthesized with F127 as the encapsulation matrix which absorb 1550 nm excitation light and have three-photon fluorescence beneath the skull of a mouse. Printed with permission from American Chemical Society [171]. (D) Eu(III)-complexes surface-modified AuNPs as contract agents for 3D imaging of microdamaged bones with two-photon fluorescence imaging, after being immersed for 4 h in AuNPs. Printed with permission from Elsevier [173].

the two-photon signal from a single AuNR through *in vivo* imaging of mouse ear blood vessels was found to be 58 times that of the two-photon fluorescence signal from a single rhodamine molecule [166]. Additionally, the two-photon signal was found to be three orders of magnitude brighter in AuNR labeled cancer cells than the two-photon autofluorescence emission intensity from unlabeled cancer cells [32]. Besides AuNRs, the SPR of gold nanostars can also be tuned into the NIR region in order to display a strong two-photon luminescence both *in vitro* and *in vivo*, and the SPR intensifies with increasing branch number, branch length, and overall star size [167]. As the efficacy of TPI is greatly dependent on the shapes of the AuNPs, Gao et al. examined five different shapes (nanospheres, nanocubes, nanotriangles, nanorods, and nanostars) with similar sizes. Their results showed that the TPI intensity increases in the order of nanospheres, nanocubes, nanotriangles, nanorods, and nanostars, where the TPI intensity of gold nanostar is 50,000 times higher than that of the gold nanosphere (Fig. 12B) [168].

To develop new types of two-photon (or multi-photon) contrast agents other than the typically used AuNRs, Park et al. synthesized 100 nm porous AuNPs to enhance the SPR in two-photon luminescence by 20 times compared to AuNRs [169]. In addition, Yin et al. developed core–shell and dumbbell Gd-tailored AuNRs that exhibited good TPI efficacy [170]. Wang et al. fabricated an aggregation-induced emission luminogen with a large three-photon absorption cross section at deep-red emission at 1550 nm. This technique can image mouse cerebral vasculature without having to perform a craniotomy and skull-thinning that are usually required for TPI; blood vessels of 2.4 μm can still be recognized at least 300 μm beneath the skull (Fig. 12C) [171]. A similar strategy using aggregation-induced emission nanoparticles as photosensitizers demonstrated the ability of these nanoparticles in assisting TPI at 1040 nm [172]. In addition, AuNPs and TPI can also be applied to detect microdamaged bones. Gunnlaugsson and co-workers developed a TPI agent based on Eu(III)-complexes that linked to the surface of AuNPs through covalent spacers (Fig. 12D). This agent can selectively bind to exposed calcium sites (*i.e.* the microcracks) inside the damaged bone surface and enable the 3D imaging of microdamaged bones [173].

Optical coherence tomography (OCT) imaging

Tomography uses sliced images of objects to generate 3D structures. The optical tomographic techniques can provide a non-invasive diagnosis without harmful irradiation such as that from X-rays. OCT is based on light interference in which a beam is split into two, one of them travelling through the sample and the other used as a reference (Fig. 13A) [174]. The time-of-flight information of a photon transmitted through or reflected from tissue contains the spatial information regarding the microstructure of the tissue [175]. The resulting interference produces a 2D image that contains the information of internal tissue microstructure. OCT deeply penetrates into the entity of interest, so it is especially useful for imaging biological tissues like the eyes, skin, or breast.

AuNP-assisted OCT could be used to detect and image the chemical environment, such as the pH and ozone concentration, in the tissue samples. Zhou et al. introduced gold triangular nanoprism core/polyaniline shell nanoparticles (GTNPs@PANI) as OCT contrast agents that is pH-responsive and possesses different extinction and scattering properties in acidic and basic environments with a response time less than 1.0 s. This technique can be used for the 3D imaging of pH distribution in biological samples, such as the acidic tumor regions [176]. In addition, their group also designed

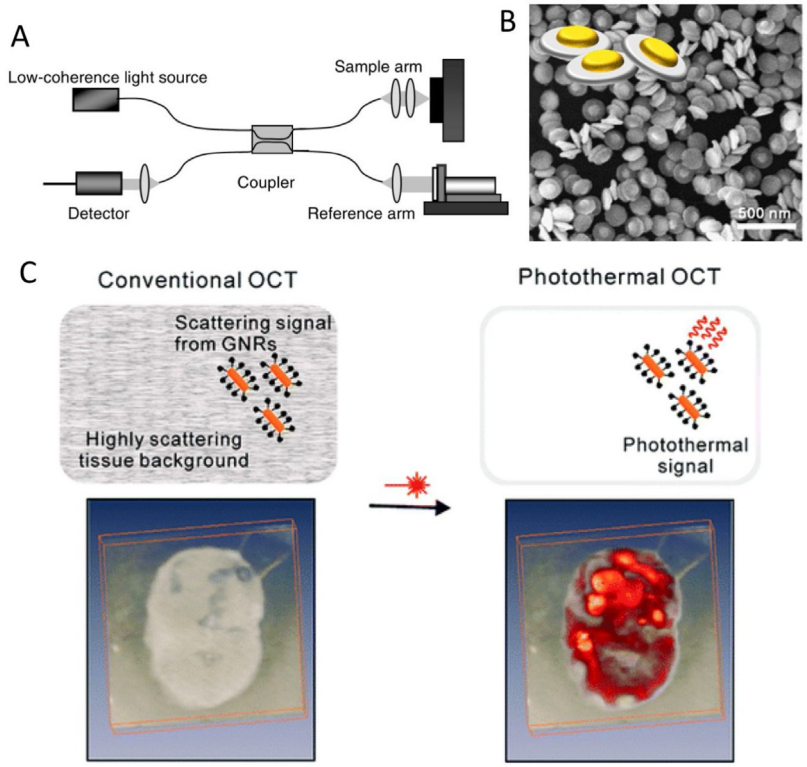

Fig. 13. (A) Optical coherence tomography (OCT) imaging working principle. Printed with permission from Springer Nature [174]. (B) Nanodisk for enhancing OCT. Printed with permission from American Chemical Society [178]. (C) OCT gets higher signal enhancement in sentinel lymph nodes (SLN) when using the Photothermal effect of AuNRs. Printed with permission from American Chemical Society [181].

similar gold triangular nanoprism platform for imaging ozone (O_3) in tissues, and quantitatively measured the penetration depth of O_3 into the anterior chamber of the fish eye [177].

New types of gold nanostructures have been developed to enhance the contrast in OCT imaging. Wi et al. fabricated two layer-stacked gold nanodisks that have a smaller nanodisk laid above a bigger nanodisk. These unique gold nanodiskes can be used for photoacoustic and optical coherence imaging (Fig. 13B) [178]. Gao et al. fabricated gold nanocups *via* a novel confined-space thermal dewetting strategy, which can be used as a new type of OCT contrast agent [179].

To study the behavior of AuNPs *in vivo*, Chhetri et al. demonstrated the use of OCT to monitor the diffusion of AuNRs (the nanotopology) into complex biological fluids and tissues. They used this technique to study nanotopological changes during extracellular matrix (ECM) remodeling (which is important in carcinogenesis), and the dehydration of pulmonary mucus [180]. Jung et al. imaged AuNRs uptake in the sentinel lymph nodes (SLN) of mice, using the photothermal effect of AuNRs that improves the OCT images. The different AuNRs accumulation patterns within several SLN structures, their concentration, and their time-dependent uptake were visualized with this photothermal OCT technique (Fig. 13C) [181]. In a work demonstrated by Prasad group, AuNPs that were produced *in situ* were used as contract agents for dentistry [182].

Photoacoustic (PA) imaging

The principle of PA imaging is based on ultrasound waves, which are generated by the thermally induced elastic expansion caused by nanosecond-range photon pulses propagating through tissue. The ultrasound waves can reach up to 7 cm in depth [183]. Compared to other NIR dyes, which are usually cleared up quickly by the body, AuNPs are more stable and have anti-photobleaching properties [184]. Köker et al. used different split-florescent protein (FP) fragments to control the assembly of plasmonic NPs into PA and SERS probes with well-defined hot spot geometry with nanogap sizes that are shaped by the precise orientation of the FP β-barrel structure, yielding strong PA signal amplifications with multimodality abilities (Fig. 14B) [185]. Galanzha et al. introduced a super-bright 22-nm spaser (surface plasmon amplification by stimulated emission of radiation, plasmonic nanolaser) with the formation of a dynamic vapor nanobubble around the spaser that has the ability to generate a stimulated emission directly inside living cells and animal tissues with emission intensity and spectral width 4100 times brighter and 30-fold narrower, respectively, than that generated from quantum dots (Fig. 14B) [186]. In addition, Chen et al. developed a single-wavelength PA dynamic contrast-enhanced imaging technique by employing a stimuli-responsive contrast agent that can generate up to 30 times stronger PA signals than the concentration-matched inorganic nanoparticle counterparts. The authors claimed that this method could increase signals more than five-fold in image contrast to *in vivo* methods (Fig. 14C and D) [187].

Conclusion and future outlook

This review provides a survey of the recent advances regarding the use of AuNPs and optical imaging together for application in biological and clinical studies. After the massive development in the synthesis and surface modification of AuNPs for decades, we now have gained great knowledge of this type of nanoparticle. Various types of AuNPs have been experimentally and theoretically studied for their optical properties and biological applications. Nonetheless, there are still many challenges, issues and opportunities for further

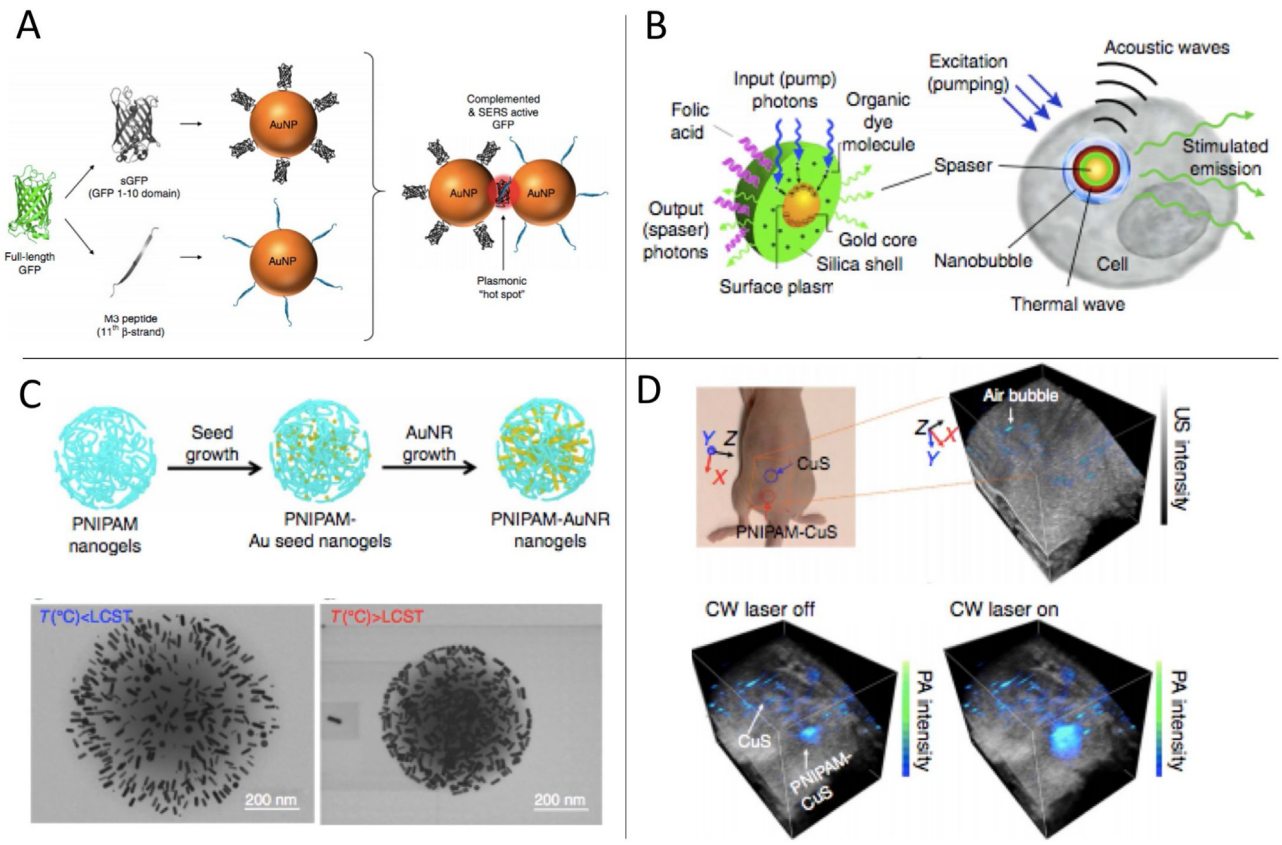

Fig. 14. (A) Schematic of assembly of AuNPs by green fluorescent protein (GFP) and M3 peptide fragments to form hot-spot SERS and photoacoustic nanoprobes. Printed with permission from Springer Nature [185]. (B) Schematic of spacer for PA imaging. Printed with permission from Springer Nature [186]. (C and D) poly (n-isopropyl acrylamide) (PNIPAM)-AuNR for enhancing PA signal. (C) The schematic and transmission electron microscope (TEM) characterization of PNIPAM-AuNR below or above the lower critical solution temperature (LCST). (D) A model mouse with both Copper Sulfide nanospheres (CuS NSs) and PNIPAM-CuS injected. The PNIPAM-CuS exhibits dramatically enhanced intensity compared with CuS. C and D are printed with permission from Springer Nature [187].

exploration in this field. On the technological development side, the following improvements are desirable.

(1) While 2D single particle tracking (SPT) techniques are well established, 3D SPT remains challenging. However, in most occasions, 3D information is much needed in order to recover the bio-nano interaction accurately. In general, 3D SPT techniques rely on simultaneously recording multiple images or manipulating the point spread function. Significant amounts of effort have been dedicated towards the development of 3D SPT for bio-nano interaction [70,188–192]. Future development is still needed to provide the multi-particle 3D tracking ability with expanded tracking range (from a few micrometers in depth to the whole cell thickness) and suB–Diffraction-limited resolution.

(2) The spatial-temporal distribution of nanoparticles in cells can be monitored with several microscopic methods with high resolution. However, due to the plasmon coupling effect, it is difficult to discern the small distances between adjacent AuNPs [129], resulting in large uncertainties in the localization of AuNPs. To measure the inter-particle distances, one strategy involves using "plasmon rulers" with high sensitivity. The plasmon ruler is based on the spectra-shift of the SPR when two plasmonic AuNPs approach each other with sensitive color changes under the microscope. Although the SPR shifting is regarded as a sensitive detection of the distance change of AuNP-labeled molecules in live cells, concerns arise as the red-shift of the SPR peak could also result from AuNPs aggregation, which complicates the detection of biomolecules.

(3) Traditional methods of AuNP fabrication are usually based on seed growth methods or lithography. Recently, new breakthroughs such as the usage of DNA self-assembly for synthesizing plasmonic gold structures in literally any size and shape [193–196] provide new possibilities for fabricating ultra-sensitive hot-spots for single-molecule imaging by SERS and PEF.

(4) Advanced scattering or fluorescence-based imaging techniques with increased signal-to-noise ratios and resolution can be coupled with other technological innovations to further improve imaging capabilities of AuNPs *in vivo*. However, the practical application of *in vivo* imaging is still difficult due to the low penetration depth of the scattered light in tissue samples. To lower the scattering background and improve the detection depth, AuNPs that scatter NIR light (such as AuNRs, core-shell AuNPs, *etc.*), especially in the NIR II window (1000–1700 nm), should be developed and used [197].

On the application side, there are also major challenges: First, it is difficult to acquire the fundamental understanding of bio-nano interactions in complex biological environments. While most of the past and current studies focus on observing the nanoparticles' behaviors in internalization, transport and bio-distribution, the detailed mechanism of how the nanoparticles interact with different biomacromolecules, such as proteins, and how they trigger the subsequent biological response is still unknown. The advancement of the super-resolution microscopic techniques is promising in shining a light on the basic understanding of this process in real time. Second, the clinical application is still lacking, which requires

more information on the long-term toxicity of AuNPs *in vivo*. The safety of AuNPs in clinical use is still questionable. However, several recent reports estimated the toxicity of AuNPs in mice that seems to accumulate in the liver and spleen, but no obvious toxicity effect is observable [198].

Declarations of interest

None.

Acknowledgments

We thank Arusha Siddiqa and Tsion Assey for their great help with this review article. We also thank Paige Warner and Seth L. Filbrun for their great help in proof-reading the manuscript. Y.W., M.R.K.A. and M.A.E. acknowledge the National Science Foundation Division of Chemistry (CHE) Grant 1608801 for its support of this work. K.C. and N.F. acknowledge funding support from National Science Foundation (CBET-1604612).

References

[1] P.K. Jain, K.S. Lee, I.H. El-Sayed, M.A. El-Sayed, J. Phys. Chem. B 110 (2006) 7238–7248.
[2] M.C. Daniel, D. Astruc, Chem. Rev. 104 (2004) 293–346.
[3] M. Faraday, Philos. Trans. R. Soc. London 147 (1857) 145–181.
[4] B. Nikoobakht, M. El-Sayed, Chem. Mater. 15 (2003) 1957–1962.
[5] C.J. Murphy, T.K. Sau, A.M. Gole, C.J. Orendorff, J. Gao, L. Gou, S.E. Hunyadi, T. Li, J. Phys. Chem. B 109 (2005) 13857–13870.
[6] E.C. Dreaden, A.M. Alkilany, X. Huang, C.J. Murphy, M.A. El-Sayed, Chem. Soc. Rev. 41 (2012) 2740–2779.
[7] M. Hu, J. Chen, Z.Y. Li, L. Au, G.V. Hartland, X. Li, M. Marquez, Y. Xia, Chem. Soc. Rev. 35 (2006) 1084–1094.
[8] M.R. Ali, B. Snyder, M.A. El-Sayed, Langmuir 28 (2012) 9807–9815.
[9] Y. Sun, Y. Xia, Science 298 (2002) 2176–2179.
[10] O. Neumann, A.S. Urban, J. Day, S. Lal, P. Nordlander, N.J. Halas, ACS Nano 7 (2013) 42–49.
[11] C.J. Murphy, A.M. Gole, S.E. Hunyadi, J.W. Stone, P.N. Sisco, A. Alkilany, B.E. Kinard, P. Hankins, Chem. Commun. (Camb.) (2008) 544–557.
[12] M.R. Ali, I.M. Ibrahim, H.R. Ali, S.A. Selim, M.A. El-Sayed, Int. J. Nanomed. 11 (2016) 4849–4863.
[13] M.R.K. Ali, Y. Wu, Y. Tang, H. Xiao, K. Chen, T. Han, N. Fang, R. Wu, M.A. El-Sayed, Proc. Natl. Acad. Sci. U. S. A. 114 (2017) E5655–E5663.
[14] M. Turner, V.B. Golovko, O.P. Vaughan, P. Abdulkin, A. Berenguer-Murcia, M.S. Tikhov, B.F. Johnson, R.M. Lambert, Nature 454 (2008) 981–983.
[15] X. Huang, M.A. El-Sayed, J. Adv. Res. 1 (2010) 13–28.
[16] A.K. Oyelere, P.C. Chen, X. Huang, I.H. El-Sayed, M.A. El-Sayed, Bioconjug. Chem. 18 (2007) 1490–1497.
[17] D. Dam, J. Lee, P. Sisco, D. Co, M. Zhang, M. Wasielewski, T. Odom, ACS Nano 6 (2012) 3318–3326.
[18] S. Eustis, M.A. el-Sayed, Chem. Soc. Rev. 35 (2006) 209–217.
[19] C.J. Murphy, A.M. Gole, J.W. Stone, P.N. Sisco, A.M. Alkilany, E.C. Goldsmith, S.C. Baxter, Acc. Chem. Res. 41 (2008) 1721–1730.
[20] R. Bardhan, S. Lal, A. Joshi, N.J. Halas, Acc. Chem. Res. 44 (2011) 936–946.
[21] E.C. Cho, C. Glaus, J. Chen, M.J. Welch, Y. Xia, Trends Mol. Med. 16 (2010) 561–573.
[22] S. Maier, M. Brongersma, P. Kik, S. Meltzer, A. Requicha, H. Atwater, Adv. Mater. 13 (2001) 1501-+.
[23] M.A. van Dijk, A.L. Tchebotareva, M. Orrit, M. Lippitz, S. Berciaud, D. Lasne, L. Cognet, B. Lounis, Phys. Chem. Chem. Phys. 8 (2006) 3486–3495.
[24] V. Myroshnychenko, J. Rodríguez-Fernández, I. Pastoriza-Santos, A.M. Funston, C. Novo, P. Mulvaney, L.M. Liz-Marzán, F.J. García de Abajo, Chem. Soc. Rev. 37 (2008) 1792–1805.
[25] S. Nie, S. Emery, Science 275 (1997) 1102–1106.
[26] L. Opilik, T. Schmid, R. Zenobi, Annu. Rev. Anal. Chem. Palo Alto Calif (Palo Alto Calif) 6 (2013) 379–398.
[27] J.F. Li, C.Y. Li, R.F. Aroca, Chem. Soc. Rev. 46 (2017) 3962–3979.
[28] J.R. Lakowicz, K. Ray, M. Chowdhury, H. Szmacinski, Y. Fu, J. Zhang, K. Nowaczyk, Analyst 133 (2008) 1308–1346.
[29] M. Bauch, K. Toma, M. Toma, Q. Zhang, J. Dostalek, Plasmonics 9 (2014) 781–799.
[30] Y. Gu, W. Sun, G. Wang, N. Fang, J. Am. Chem. Soc. 133 (2011) 5720–5723.
[31] A.G. Tkachenko, H. Xie, Y. Liu, D. Coleman, J. Ryan, W.R. Glomm, M.K. Shipton, S. Franzen, D.L. Feldheim, Bioconjug. Chem. 15 (2004) 482–490.
[32] N.J. Durr, T. Larson, D.K. Smith, B.A. Korgel, K. Sokolov, A. Ben-Yakar, Nano Lett. 7 (2007) 941–945.
[33] P.K. Jain, X. Huang, I.H. El-Sayed, M.A. El-Sayed, Acc. Chem. Res. 41 (2008) 1578–1586.
[34] C. Rosman, S. Pierrat, A. Henkel, M. Tarantola, D. Schneider, E. Sunnick, A. Janshoff, C. Sönnichsen, Small 8 (2012) 3683–3690.
[35] S.H. Wang, C.W. Lee, F.G. Tseng, K.K. Liang, P.K. Wei, J. Biophotonics (2015).
[36] M. Liu, Q. Li, L. Liang, J. Li, K. Wang, M. Lv, N. Chen, H. Song, J. Lee, J. Shi, L. Wang, R. Lal, C. Fan, Nat. Commun. 8 (2017) 15646.
[37] X. Nan, P.A. Sims, X.S. Xie, ChemPhysChem 9 (2008) 707–712.
[38] R. Schneider, T. Glaser, M. Berndt, S. Diez, Opt. Express 21 (2013) 3523–3539.
[39] W. Qian, X. Huang, B. Kang, M.A. El-Sayed,J. Biomed. Opt. 15 (2010), 046025.
[40] X.Y. Wan, L.L. Zheng, P.F. Gao, X.X. Yang, C.M. Li, Y.F. Li, C.Z. Huang, Sci. Rep. 4 (2014) 4529.
[41] G. Rong, H. Wang, L.R. Skewis, B.M. Reinhard, Nano Lett. 8 (2008) 3386–3393.
[42] B. Xiong, Z. Huang, H. Zou, C. Qiao, Y. He, E.S. Yeung, ACS Nano 11 (2017) 541–548.
[43] D. Riveline, E. Zamir, N.Q. Balaban, U.S. Schwarz, T. Ishizaki, S. Narumiya, Z. Kam, B. Geiger, A.D. Bershadsky, J. Cell Biol. 153 (2001) 1175–1186.
[44] D.R. Stabley, C. Jurchenko, S.S. Marshall, K.S. Salaita, Nat. Methods 9 (2011) 64–67.
[45] Y. Liu, K. Yehl, Y. Narui, K. Salaita, J. Am. Chem. Soc. 135 (2013) 5320–5323.
[46] K. Lee, Y. Cui, L.P. Lee, J. Irudayaraj, Nat. Nanotechnol. 9 (2014) 474–480.
[47] C. Lambertz, A. Martos, A. Henkel, A. Neiser, T.T. Kliesch, A. Janshoff, P. Schwille, C. Sönnichsen, Nano Lett. 16 (2016) 3540–3544.
[48] L. Zhang, Y. Li, D.W. Li, C. Jing, X. Chen, M. Lv, Q. Huang, Y.T. Long, I. Willner, Angew. Chem. Int. Ed. Engl. 50 (2011) 6789–6792.
[49] Y. Liu, J.R. Ashton, E.J. Moding, H. Yuan, J.K. Register, A.M. Fales, J. Choi, M.J. Whitley, X. Zhao, Y. Qi, Y. Ma, G. Vaidyanathan, M.R. Zalutsky, D.G. Kirsch, C.T. Badea, T. Vo-Dinh, Theranostics 5 (2015) 946–960.
[50] E.D. SoRelle, O. Liba, J.L. Campbell, R. Dalal, C.L. Zavaleta, A. de la Zerda, Elife 5 (2016).
[51] O. Betzer, N. Perets, A. Angel, M. Motiei, T. Sadan, G. Yadid, D. Offen, R. Popovtzer, ACS Nano 11 (2017) 10883–10893.
[52] C. Sonnichsen, B. Reinhard, J. Liphardt, A. Alivisatos, Nat. Biotechnol. 23 (2005) 741–745.
[53] Y. Cui, J. Irudayaraj, Wiley Interdiscip. Rev. Nanomed. Nanobiotechnol. 7 (2015) 387–407.
[54] H. Ueno, S. Nishikawa, R. Iino, K.V. Tabata, S. Sakakihara, T. Yanagida, H. Noji, Biophys. J. 98 (2010) 2014–2023.
[55] P. Zhang, S. Lee, H. Yu, N. Fang, S.H. Kang, Sci. Rep. 5 (2015) 11447.
[56] X. Cheng, X. Cao, B. Xiong, Y. He, E. Yeung, Nano Res. 10 (2017) 1423–1433.
[57] K. Chen, Graduate Theses and Dissertations (2015) https://lib.dr.iastate.edu/etd/14777).
[58] M. Tsunoda, D. Isailovic, E.S. Yeung, J. Micro. 232 (2008) 207–211.
[59] J. Zhu, J. He, J.Y. Chen, D.-R. Lu, L. Zhou, SPIE (2008) 3.
[60] E.D. Salmon, P. Tran, High-Resolution video-enhanced differential interference contrast light microscopy, in: L. Wilson, P. Matsudaira (Eds.), Methods in Cell Biology, Academic Press, 2003, pp. 289–318.
[61] N.E. Ziv, J. Schiller, CSH Protoc. 2007 (2007), pdb prot4787.
[62] A.S. Stender, K. Marchuk, C. Liu, S. Sander, M.W. Meyer, E.A. Smith, B. Neupane, G. Wang, J. Li, J.X. Cheng, B. Huang, N. Fang, Chem. Rev. 113 (2013) 2469–2527.
[63] W. Sun, G. Wang, N. Fang, E.S. Yeung, Anal. Chem. 81 (2009) 9203–9208.
[64] B.D. Chithrani, W.C. Chan, Nano Lett. 7 (2007) 1542–1550.
[65] M. Ali, Y. Wu, D. Ghosh, B. Do, K. Chen, M. Dawson, N. Fang, T. Sulchek, M. El-Sayed, ACS Nano 11 (2017) 3716–3726.
[66] F. Zhao, K. Chen, B. Dong, K. Yang, Y. Gu, N. Fang, Opt. Express 25 (2017) 9860–9871.
[67] J. Chen, Y. Xu, X. Lv, X. Lai, S. Zeng, Opt. Express 21 (2013) 112–121.
[68] Y. Gu, X. Di, W. Sun, G. Wang, N. Fang, Anal. Chem. (2012).
[69] Y. Gu, G. Wang, N. Fang, ACS Nano 7 (2013) 1658–1665.
[70] K. Chen, Y. Gu, W. Sun, Bin Dong, G. Wang, X. Fan, T. Xia, N. Fang, Nat. Commun. 8 (2017) 887.
[71] A.E. Augspurger, A.S. Stender, R. Han, N. Fang, Anal. Chem. 86 (2014) 1196–1201.
[72] P. Kukura, H. Ewers, C. Müller, A. Renn, A. Helenius, V. Sandoghdar, Nat. Methods 6 (2009) 923–927.
[73] J. Ortega-Arroyo, P. Kukura, Phys. Chem. Chem. Phys. 14 (2012) 15625–15636.
[74] K.J. Mickolajczyk, N.C. Deffenbaugh, J.O. Arroyo, J. Andrecka, P. Kukura, W.O. Hancock, Proc Natl Acad Sci U S A 112 (2015) E7186–7193.
[75] J. Andrecka, Y. Takagi, K. Mickolajczyk, L. Lippert, J. Sellers, W. Hancock, Y. Goldman, P. Kukura, M. Spies, Y. Chemla, Single-Molecule Enzymology: Fluorescence-Based and High-Throughput Methods, vol 581, 2016, pp. 517–539.
[76] K.J. Mickolajczyk, E.A. Geyer, T. Kim, L.M. Rice, W.O. Hancock,bioRxiv (2018), 418053.
[77] C.L. Hsieh, S. Spindler, J. Ehrig, V. Sandoghdar, J. Phys. Chem. B 118 (2014) 1545–1554.
[78] H.M. Wu, Y.H. Lin, T.C. Yen, C.L. Hsieh, Sci. Rep. 6 (2016) 20542.
[79] D. Nedosekin, E. Galanzha, E. Dervishi, A. Biris, V. Zharov, Small 10 (2014) 135–142.
[80] D. Boyer, P. Tamarat, A. Maali, B. Lounis, M. Orrit, Science 297 (2002) 1160–1163.
[81] G. Wang, W. Sun, Y. Luo, N. Fang, J. Am. Chem. Soc. 132 (2010) 16417–16422.
[82] Y. Gu, W. Sun, G. Wang, K. Jeftinija, S. Jeftinija, N. Fang, Nat. Commun. 3 (2012) 1030.
[83] J.W. Ha, K. Chen, N. Fang, Chem. Commun. (Camb.) 49 (2013) 11038–11040.
[84] K. Chen, C.C. Lin, J. Vela, N. Fang, Anal. Chem. 87 (2015) 4096–4099.

[85] G.W. Kim, J.W. Ha, Anal. Sci. 33 (2017) 1021–1025.
[86] G.W. Kim, J.W. Ha, J. Phys. Chem. C 121 (2017) 19975–19982.
[87] S.Y. Lee, Y. Han, J.W. Hong, J.W. Ha, Nanoscale 9 (2017) 12060–12067.
[88] W. Sun, Y. Gu, G. Wang, N. Fang, Anal. Chem. 84 (2012) 1134–1138.
[89] S.K. Chakkarapani, Y. Sun, S. Lee, N. Fang, S.H. Kang, ACS Nano 12 (2018) 4156–4163.
[90] C. Sönnichsen, A.P. Alivisatos, Nano Lett. 5 (2005) 301–304.
[91] D. Spetzler, J. York, D. Daniel, R. Fromme, D. Lowry, W. Frasch, Biochemistry 45 (2006) 3117–3124.
[92] D. Xu, Y. He, E.S. Yeung, Anal. Chem. 86 (2014) 3397–3404.
[93] L. Xiao, Y. Qiao, Y. He, E.S. Yeung, Anal. Chem. 82 (2010) 5268–5274.
[94] S. Enoki, R. Iino, Y. Niitani, Y. Minagawa, M. Tomishige, H. Noji, Anal. Chem. 87 (2015) 2079–2086.
[95] L. Kaplan, A. Ierokomos, P. Chowdary, Z. Bryant, B. Cui, Sci. Adv. 4 (2018).
[96] P.D. Chowdary, L. Kaplan, D.L. Che, B. Cui, Biophys. J. 115 (2018) 230–241.
[97] J.W. Ha, K. Marchuk, N. Fang, Nano Lett. 12 (2012) 4282–4288.
[98] W.-S. Chang, J.W. Ha, L.S. Slaughter, S. Link, Proc. Natl. Acad. Sci. 107 (2010) 2781–2786.
[99] J. Zhang, Y. Huang, C.-J. Chuang, M. Bivolarska, C.W. See, M.G. Somekh, M.C. Pitter, Opt. Express 19 (2011) 2643–2648.
[100] A. Tcherniak, S. Dominguez-Medina, W.-S. Chang, P. Swanglap, L.S. Slaughter, C.F. Landes, S. Link, J. Phys. Chem. C 115 (2011) 15938–15949.
[101] B. Zhang, T. Lan, X. Huang, C. Dong, J. Ren, Anal. Chem. 85 (2013) 9433–9438.
[102] C.J. Behrend, J.N. Anker, B.H. McNaughton, M. Brasuel, M.A. Philbert, R. Kopelman, J. Phys. Chem. B 108 (2004) 10408–10414.
[103] Y. Yi, L. Sanchez, Y. Gao, Y. Yu, Analyst 141 (2016) 3526–3539.
[104] S.M. Anthony, Y. Yu, Anal. Methods 7 (2015) 7020–7028.
[105] Y. Gao, S.M. Anthony, Y. Yi, W. Li, Y. Yu, Y. Yu, Langmuir 34 (2018) 1151–1158.
[106] I. Lee, H. Moon, J. Joo, K. Kim, S. Hong, M. Cho, ACS Photon. 5 (2018) 797–804.
[107] J.F. Li, Y.F. Huang, Y. Ding, Z.L. Yang, S.B. Li, X.S. Zhou, F.R. Fan, W. Zhang, Z.Y. Zhou, D.Y. Wu, B. Ren, Z.L. Wang, Z.Q. Tian, Nature 464 (2010) 392–395.
[108] K.L. Wustholz, A.I. Henry, J.M. McMahon, R.G. Freeman, N. Valley, M.E. Piotti, M.J. Natan, G.C. Schatz, R.P. Van Duyne, J. Am. Chem. Soc. 132 (2010) 10903–10910.
[109] F. De Angelis, F. Gentile, F. Mecarini, G. Das, M. Moretti, P. Candeloro, M. Coluccio, G. Cojoc, A. Accardo, C. Liberale, R. Zaccaria, G. Perozziello, L. Tirinato, A. Toma, G. Cuda, R. Cingolani, E. Di Fabrizio, Nat. Photonics 5 (2011) 683–688.
[110] S. Yang, X. Dai, B. Stogin, T. Wong, Proc. Natl. Acad. Sci. U. S. A. 113 (2016) 268–273.
[111] S. Tanwar, K.K. Haldar, T. Sen, J. Am. Chem. Soc. 139 (2017) 17639–17648.
[112] P. Zhan, T. Wen, Z.G. Wang, Y. He, J. Shi, T. Wang, X. Liu, G. Lu, B. Ding, Angew. Chem. Int. Ed. Engl. 57 (2018) 2846–2850.
[113] J. Ando, K. Fujita, N.I. Smith, S. Kawata, Nano Lett. 11 (2011) 5344–5348.
[114] K.C. Huang, K. Bando, J. Ando, N.I. Smith, K. Fujita, S. Kawata, Methods 68 (2014) 348–353.
[115] M.R. Ali, Y. Wu, T. Han, X. Zang, H. Xiao, Y. Tang, R. Wu, F.M. Fernández, M.A. El-Sayed, J. Am. Chem. Soc. 138 (2016) 15434–15442.
[116] C. Sun, M. Gao, X. Zhang, Anal. Bioanal. Chem. 409 (2017) 4915–4926.
[117] R. Lahr, P. Vikesland, ACS Sustain. Chem. Eng. 2 (2014) 1599–1608.
[118] X. Qian, X.H. Peng, D.O. Ansari, Q. Yin-Goen, G.Z. Chen, D.M. Shin, L. Yang, A.N. Young, M.D. Wang, S. Nie, Nat. Biotechnol. 26 (2008) 83–90.
[119] Y. Wang, S. Kang, A. Khan, G. Ruttner, S.Y. Leigh, M. Murray, S. Abeytunge, G. Peterson, M. Rajadhyaksha, S. Dintzis, S. Javid, J.T. Liu, Sci. Rep. 6 (2016) 21242.
[120] L. Sinha, Y. Wang, C. Yang, A. Khan, J.G. Brankov, J.T. Liu, K.M. Tichauer, Sci. Rep. 5 (2015) 8582.
[121] M.F. Kircher, A. de la Zerda, J.V. Jokerst, C.L. Zavaleta, P.J. Kempen, E. Mittra, K. Pitter, R. Huang, C. Campos, F. Habte, R. Sinclair, C.W. Brennan, I.K. Mellinghoff, E.C. Holland, S.S. Gambhir, Nat. Med. 18 (2012) 829–834.
[122] M.F. Kircher, Nanomedicine (Lond.) 12 (2017) 171–174.
[123] N. Stone, K. Faulds, D. Graham, P. Matousek, Anal. Chem. 82 (2010) 3969–3973.
[124] G. von Maltzahn, A. Centrone, J.H. Park, R. Ramanathan, M.J. Sailor, T.A. Hatton, S.N. Bhatia, Adv Mater 21 (2009) 3175–3180.
[125] J. Qian, L. Jiang, F. Cai, D. Wang, S. He, Biomaterials 32 (2011) 1601–1610.
[126] J.W. Kang, P.T. So, R.R. Dasari, D.K. Lim, Nano Lett. 15 (2015) 1766–1772.
[127] N. Gandra, S. Singamaneni, Adv Mater 25 (2013) 1022–1027.
[128] J. GERSTEN, A. NITZAN, J. Chem. Phys. 75 (1981) 1139–1152.
[129] K.A. Willets, A.J. Wilson, V. Sundaresan, P.B. Joshi, Chem. Rev. 117 (2017) 7538–7582.
[130] S. Kühn, U. Håkanson, L. Rogobete, V. Sandoghdar,Phys. Rev. Lett. 97 (2006), 017402.
[131] H. Yuan, S. Khatua, P. Zijlstra, M. Yorulmaz, M. Orrit, Angew. Chem. Int. Ed. Engl. 52 (2013) 1217–1221.
[132] J. Xie, Y. Zheng, J.Y. Ying, J. Am. Chem. Soc. 131 (2009) 888–889.
[133] H.H. Wang, C.A. Lin, C.H. Lee, Y.C. Lin, Y.M. Tseng, C.L. Hsieh, C.H. Chen, C.H. Tsai, C.T. Hsieh, J.L. Shen, W.H. Chan, W.H. Chang, H.I. Yeh, ACS Nano 5 (2011) 4337–4344.
[134] J.N. Farahani, D.W. Pohl, H.J. Eisler, B. Hecht,Phys. Rev. Lett. 95 (2005), 017402.
[135] A. Kinkhabwala, Z. Yu, S. Fan, Y. Avlasevich, K. Mullen, W. Moerner, Nat. Photonics 3 (2009) 654–657.
[136] S. Khatua, P. Paulo, H. Yuan, A. Gupta, P. Zijlstra, M. Orrit, ACS Nano 8 (2014) 4440–4449.
[137] E. Wientjes, J. Renger, A.G. Curto, R. Cogdell, N.F. van Hulst, Nat. Commun. 5 (2014) 4236.
[138] G. Akselrod, C. Argyropoulos, T. Hoang, C. Ciraci, C. Fang, J. Huang, D. Smith, M. Mikkelsen, Nat. Photon. 8 (2014) 835–840.
[139] A.A. Al Balushi, A. Zehtabi-Oskuie, R. Gordon, Biomed. Opt. Express 4 (2013) 1504–1511.
[140] R. Regmi, A.A. Al Balushi, H. Rigneault, R. Gordon, J. Wenger, Sci. Rep. 5 (2015) 15852.
[141] A. Kotnala, R. Gordon, Nano Lett. 14 (2014) 853–856.
[142] J. de Torres, M. Mivelle, S.B. Moparthi, H. Rigneault, N.F. Van Hulst, M.F. García-Parajó, E. Margeat, J. Wenger, Nano Lett. 16 (2016) 6222–6230.
[143] S. Masuda, Y. Yanase, E. Usukura, S. Ryuzaki, P. Wang, K. Okamoto, T. Kuboki, S. Kidoaki, K. Tamada, Sci. Rep. 7 (2017) 3720.
[144] J.C.G. Jeynes, K. Geraki, C. Jeynes, M. Zhaohong, A.A. Bettiol, E. Latorre, L.W. Harries, C. Soeller, ACS Nano 11 (2017) 12632–12640.
[145] A. Taylor, R. Verhoef, M. Beuwer, Y. Wang, P. Zijlstra, J. Phys. Chem. C Nanomater. Interfaces 122 (2018) 2336–2342.
[146] N. Feiner-Gracia, M. Beck, S. Pujals, S. Tosi, T. Mandal, C. Buske, M. Linden, L. Albertazzi, Small 13 (2017).
[147] A. Jaworska, T. Wojcik, K. Malek, U. Kwolek, M. Kepczynski, A.A. Ansary, S. Chlopicki, M. Baranska, Microchim. Ichnoanal. Acta 182 (2014) 119–127.
[148] Y. Zhang, Y. Chen, J. Yu, D.J.S. Birch, (2017) 13th IASTED International Conference on Biomedical Engineering (BioMed). https://ieeexplore.ieee.org/document/7893264.
[149] P. Huang, J. Lin, S. Wang, Z. Zhou, Z. Li, Z. Wang, C. Zhang, X. Yue, G. Niu, M. Yang, D. Cui, X. Chen, Biomaterials 34 (2013) 4643–4654.
[150] B. Jang, J.-Y. Park, C.-H. Tung, I.-H. Kim, Y. Choi, ACS Nano 5 (2011) 1086–1094.
[151] K. Hayashi, M. Nakamura, H. Miki, S. Ozaki, M. Abe, T. Matsumoto, K. Ishimura, Chem. Commun. 49 (2013) 5334.
[152] J. Zheng, P.R. Nicovich, R.M. Dickson, Annu. Rev. Phys. Chem. 58 (2007) 409–431.
[153] L. Chen, C. Wang, Z. Yuan, H. Chang, Anal. Chem. 87 (2015) 216–229.
[154] X. Qu, Y. Li, L. Li, Y. Wang, J. Liang, J. Liang,. (2015).
[155] S. Palmal, N. Jana, Wiley Interdiscip. Rev.-Nanomed. Nanobiotechnol. 6 (2014) 102–110.
[156] V. Venkatesh, A. Shukla, S. Sivakumar, S. Verma, ACS Appl. Mater. Interfaces 6 (2014) 2185–2191.
[157] X. Wang, Y. Wang, H. He, X. Ma, Q. Chen, S. Zhang, B. Ge, S. Wang, W.M. Nau, F. Huang, ACS Appl. Mater. Interfaces 9 (2017) 17799–17806.
[158] T. Fernandez, J. Pearson, M. Leal, M. Torres, M. Blanca, C. Mayorga, X. Le Guevel, Biomaterials 43 (2015) 1–12.
[159] S. Chandirasekar, C. Chandrasekaran, T. Muthukumarasamyvel, G. Sudhandiran, N. Rajendiran, Colloids Surf. B Biointerfaces 143 (2016) 472–480.
[160] C. Zhang, C. Li, Y. Liu, J. Zhang, C. Bao, S. Liang, Q. Wang, Y. Yang, H. Fu, K. Wang, D. Cui, Adv. Funct. Mater. 25 (2015) 1314–1325.
[161] J. Wang, G. Zhang, Q. Li, H. Jiang, C. Liu, C. Amatore, X. Wang, Sci. Rep. 3 (2013).
[162] P. Zhao, K. He, Y. Han, Z. Zhang, M. Yu, H. Wang, Y. Huang, Z. Nie, S. Yao, Anal. Chem. 87 (2015) 9998–10005.
[163] A. Yahia-Ammar, D. Sierra, F. Merola, N. Hildebrandt, X. Le Guevel, ACS Nano 10 (2016) 2591–2599.
[164] V. Ntziachristos, Nat. Methods 7 (2010) 603–614.
[165] W. Denk, J.H. Strickler, W.W. Webb, Science 248 (1990) 73–76.
[166] H. Wang, T.B. Huff, D.A. Zweifel, W. He, P.S. Low, A. Wei, J.X. Cheng, Proc. Natl. Acad. Sci. U. S. A. 102 (2005) 15752–15756.
[167] H. Yuan, C.G. Khoury, H. Hwang, C.M. Wilson, G.A. Grant, T. Vo-Dinh,Nanotechnology 23 (2012), 075102.
[168] N. Gao, Y. Chen, L. Li, Z. Guan, T. Zhao, N. Zhou, P. Yuan, S. Yao, Q. Xu, J. Phys. Chem. C 118 (2014) 13904–13911.
[169] J.H. Park, J. Park, S. Kim, S.-H. Kim, T.G. Lee, J.Y. Lee, J.-S. Wi,J. Biophoton. 11 (2018), e201870131.
[170] J. Yin, D. Chen, S. Wu, C. Li, L. Liu, Y. Shao, Nanoscale 9 (2017) 16661–16673.
[171] Y. Wang, M. Chen, N. Alifu, S. Li, W. Qin, A. Qin, B.Z. Tang, J. Qian, ACS Nano 11 (2017) 10452–10461.
[172] N. Alifu, X. Dong, D. Li, X. Sun, A. Zebibula, D. Zhang, G. Zhang, J. Qian, Mater. Chem. Front. 1 (2017) 1746–1753.
[173] E. Surender, S. Comby, B. Cavanagh, O. Brennan, T. Lee, T. Gunnlaugsson, Chem 1 (2016) 438–455.
[174] D.P. Popescu, L.P. Choo-Smith, C. Flueraru, Y. Mao, S. Chang, J. Disano, S. Sherif, M.G. Sowa, Biophys. Rev. 3 (2011) 155.
[175] D. Huang, E.A. Swanson, C.P. Lin, J.S. Schuman, W.G. Stinson, W. Chang, M.R. Hee, T. Flotte, K. Gregory, C.A. Puliafito, Science 254 (1991) 1178–1181.
[176] P. Tang, X. Jiang, Y. Wang, H. Chen, Y.S. Zhang, P. Gao, H. Wang, X. Li, J. Zhou, Anal. Chem. 89 (2017) 9758–9766.
[177] X. Jiang, P. Tang, P. Gao, Y.S. Zhang, C. Yi, J. Zhou, Anal. Chem. 89 (2017) 2561–2568.
[178] J.S. Wi, J. Park, H. Kang, D. Jung, S.W. Lee, T.G. Lee, ACS Nano 11 (2017) 6225–6232.
[179] A. Gao, W. Xu, Y. Ponce de León, Y. Bai, M. Gong, K. Xie, B.H. Park, Y. Yin, Adv. Mater. 29 (2017).
[180] R. Chhetri, R. Blackmon, W. Wu, D. Hill, B. Button, P. Casbas-Hernandez, M. Troester, J. Tracy, A. Oldenburg, Proc. Natl. Acad. Sci. U. S. A. 111 (2014) E4289–E4297.
[181] Y. Jung, R. Reif, Y. Zeng, R. Wang, Nano Lett. 11 (2011) 2938–2943.

[182] A.K. Braz, R.E. de Araujo, T.Y. Ohulchanskyy, S. Shukla, E.J. Bergey, A.S. Gomes, P.N. Prasad,J. Biomed. Opt. 17 (2012), 066003.
[183] L.V. Wang, S. Hu, Science 335 (2012) 1458–1462.
[184] W. Li, X. Chen, Nanomedicine (Lond.) 10 (2015) 299–320.
[185] T. Köker, N. Tang, C. Tian, W. Zhang, X. Wang, R. Martel, F. Pinaud, Nat. Commun. 9 (2018) 607.
[186] E.I. Galanzha, R. Weingold, D.A. Nedosekin, M. Sarimollaoglu, J. Nolan, W. Harrington, A.S. Kuchyanov, R.G. Parkhomenko, F. Watanabe, Z. Nima, A.S. Biris, A.I. Plekhanov, M.I. Stockman, V.P. Zharov, Nat. Commun. 8 (2017) 15528.
[187] Y.S. Chen, S.J. Yoon, W. Frey, M. Dockery, S. Emelianov, Nat. Commun. 8 (2017) 15782.
[188] E.P. Perillo, Y.-L. Liu, K. Huynh, C. Liu, C.-K. Chou, M.-C. Hung, H.-C. Yeh, A.K. Dunn, Nat. Commun. 6 (2015) 7874.
[189] E. Toprak, H. Balci, B.H. Blehm, P.R. Selvin, Nano Lett. 7 (2007) 2043–2045.
[190] M. Speidel, A. Jonáš, E.-L. Florin, Opt. Lett. 28 (2003) 69–71.
[191] S.R.P. Pavani, R. Piestun, Opt. Express 16 (2008) 22048–22057.
[192] B. Huang, W. Wang, M. Bates, X. Zhuang, Science 319 (2008) 810–813.
[193] W. Sun, E. Boulais, Y. Hakobyan, W.L. Wang, A. Guan, M. Bathe, P. Yin,Science 346 (2014), 1258361.
[194] X. Lan, X. Lu, C. Shen, Y. Ke, W. Ni, Q. Wang, J. Am. Chem. Soc. 137 (2015) 457–462.
[195] L. Sun, H. Lin, D.J. Park, M.R. Bourgeois, M.B. Ross, J.C. Ku, G.C. Schatz, C.A. Mirkin, Nano Lett. 17 (2017) 2313–2318.
[196] M.B. Ross, J.C. Ku, V.M. Vaccarezza, G.C. Schatz, C.A. Mirkin, Nat. Nanotechnol. 10 (2015) 453–458.
[197] J. Park, M. Kim, J. Hwang, J. Nam, Small Methods 1 (2017).
[198] M.R. Ali, M.A. Rahman, Y. Wu, T. Han, X. Peng, M.A. Mackey, D. Wang, H.J. Shin, Z.G. Chen, H. Xiao, R. Wu, Y. Tang, D.M. Shin, M.A. El-Sayed, Proc. Natl. Acad. Sci. U. S. A. 114 (2017) E3110–E3118.

Yue Wu received her B.S. in chemistry from Zhejiang University of Technology, China in 2007 and M.S. in analytical chemistry from Dalian Institute of Chemical Physics, Chinese Academy of Sciences in 2011. She is currently pursuing a PhD in analytical chemistry at Georgia Institute of Technology under the supervision of Professor Mostafa A. El-Sayed. Her current research focuses on the development of gold nanomaterials for applications related with cancer treatment and biological optical imaging.

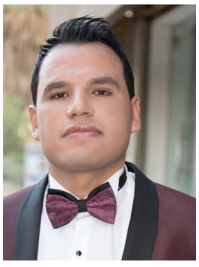

Moustafa Ali received his B.Sc and M.Sc in chemistry from Cairo University in 2005 and 2012. During his M. Sc period, he was a visiting scholar in Material Science Institute in Connecticut University. He was awarded his Ph.D. from Georgia Institute of Technology in Chemistry in the Group of Prof. El-Sayed in 2017. Currently, he is a postdoctoral Associate at the same group. His research interests include plasmonic nanoparticles synthesis, mechanistic/imaging of bio-nano interactions using spectroscopy and microscopy techniques, *etc.* His primary goal is to develop a plasmonic nanoparticle treatment for pathogens, cancer progression and metastasis.

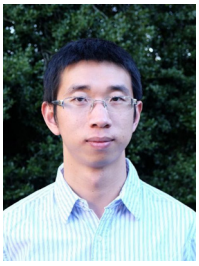

Kuangcai Chen received his B.S. degree in chemistry from Shandong University, China in 2009 and obtained his M.S. degree in analytical chemistry from Changwon National University, South Korea in 2011. He received his Ph.D. degree in analytical chemistry from Iowa State University in 2015. He is currently a Postdoctoral Research Associate at Georgia State University under the supervision of Prof. Ning Fang. His research focuses on the development of novel optical imaging methods for chemical and biophysical applications using single particle tracking and super-resolution imaging.

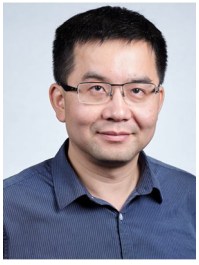

Ning Fang received his B.S. from Xiamen University, China in 1998 and his Ph.D. from the University of British Columbia, Canada in the group of Prof. David D.Y. Chen in 2006 and was a Postdoctoral Associate at Iowa State University and Ames Laboratory, US Department of Energy with Prof. Edward S. Yeung from 2006 to 2008. From 2008 to 2015, he was an Assistant Professor of Chemistry at Iowa State University and a Faculty Scientist at U.S. Department of Energy, Ames Laboratory. In July 2015, he moved his laboratory to the Department of Chemistry at Georgia State University and became an Associate Professor. His research aims to open up new frontiers in chemical and biological discovery through the development and use of novel optical imaging platforms, which provide sub-diffraction-limited spatial resolution, high angular resolution, excellent detectability, and/or nanometer localization accuracy for single molecules and nanoparticles.

Mostafa A. El-Sayed received his BSc from Ain Shams University in Egypt and his PhD from Florida State with Michael Kasha. After a research fellowship at Harvard and Cal Tech, he joined the faculty at UCLA in 1961 and Georgia Tech in 1994. He is currently the Julius Brown Chair, Regents Professor of Chemistry and Biochemistry, and the Director of the Laser Dynamics Laboratory. El-Sayed is an elected member of the U.S. National Academy of Sciences (1980), an elected Fellow of the American Academy of Arts and Sciences, an Associate member of the Third World Academy of Science, and a Fellow of the American Association for the Advancement of Science (AAAS) and of the American Physical Society. He is a former editor-in-chief of the Journal of Physical Chemistry, and recipient of the US National Medal of Science. His current research includes the optical and electronic properties of nanomaterials and their applications in sensing, nanocatalysis, and nanomedicine.